

Is chaotic advection inherent to heterogeneous Darcy flow?

Daniel Robert Lester¹ , Guy Metcalfe² , Michael Trefry³  and Marco Dentz⁴ 

¹School of Engineering, RMIT University, Melbourne, Australia

²Swinburne University of Technology, Melbourne, Australia

³Independent Researcher, Perth, Australia

⁴Spanish National Research Council (IDAEA-CSIC), 08034 Barcelona, Spain

Corresponding author: Daniel Robert Lester, daniel.lester@rmit.edu.au

(Received 1 November 2024; revised 29 July 2025; accepted 5 August 2025)

At all scales, porous materials stir interstitial fluids as they are advected, leading to complex (and chaotic) distributions of matter and energy. Of particular interest is whether porous media naturally induce chaotic advection in Darcy flows at the macroscale, as these stirring kinematics profoundly impact basic processes such as solute transport and mixing, colloid transport and deposition and chemical, geochemical and biological reactivity. While the prevalence of pore-scale chaotic advection has been established, and many studies report complex transport phenomena characteristic of chaotic advection in heterogeneous Darcy flow, it has also been shown that chaotic dynamics are prohibited in a large class of Darcy flows. In this study we rigorously establish that chaotic advection is inherent to steady three-dimensional (3-D) Darcy flow with anisotropic and heterogeneous hydraulic conductivity fields. These conductivity fields generate non-trivial braiding of streamlines, leading to both chaotic advection and (purely advective) transverse macro-dispersion. We establish that steady 3-D Darcy flow has the same topology as unsteady 2-D flow and use braid theory to establish a quantitative link between transverse dispersivity and Lyapunov exponent in heterogeneous Darcy flow. Our main results show that chaotic advection and transverse dispersion occur in both anisotropic weakly heterogeneous and in heterogeneous weakly anisotropic conductivity fields, and that the quantitative link between these phenomena persists across a broad range of conductivity fields. As the ubiquity of macroscopic chaotic advection has profound implications for the myriad processes hosted in porous media, these results call for re-evaluation of transport and reaction methods in these systems.

Key words: porous media, chaotic advection

© The Author(s), 2025. Published by Cambridge University Press. This is an Open Access article, distributed under the terms of the Creative Commons Attribution licence (<https://creativecommons.org/licenses/by/4.0/>), which permits unrestricted re-use, distribution and reproduction, provided the original article is properly cited.

1. Introduction

Porous media abound in both nature and engineered systems. From biological tissues to geological media and engineered materials, these media encompass a vast range of applications (Bear 1972; Cushman 2013). Porous materials play host to a range of fluid-borne phenomena, including mixing (Villermaux 2012; Dentz, Hidalgo & Lester 2023), dispersion (Saffman 1959; Bear 1972; Gelhar & Axness 1983; Dagan 1989), transport (Brenner & Edwards 1993) and reaction (Anna *et al.* 2013; Rolle & Le Borgne 2019; Valocchi, Bolster & Werth 2019) of colloids, chemical and biological species (Alonso-Matilla, Chakrabarti & Saintillan 2019; Dentz *et al.* 2022). These phenomena are governed by the Lagrangian kinematics of the interstitial fluid, which provide an advective template that organises the spatial structures upon which they play out. At all scales, porous materials act to stir fluids as they are advected through (Villermaux 2012; Dentz *et al.* 2023), leading to highly striated material distributions which can have profound impacts upon these fluid-borne phenomena.

For example, solute mixing and transport can be either significantly accelerated or retarded by the Lagrangian kinematics of the flow, leading to the existence of e.g. isolated fast or slow mixing regions and transport ‘barriers’ or ‘highways’ (Haller 2015; Wu *et al.* 2024). Similarly, the effective kinetics of reactive solutes are governed by transport and mixing, including the formation of reaction ‘hot spots’ due to localised fluid deformation (Rolle & Le Borgne 2019; Valocchi *et al.* 2019). It is impossible to understand, quantify and predict these processes without resolving their underlying Lagrangian kinematics (Metcalfe, Lester & Trefry 2023).

One important class of such kinematics is chaotic advection (Arnol’d 1965; Aref 1984) where fluid stirring motions (stretching and folding) yield highly striated distributions of matter and energy that can fundamentally alter these fluid-borne phenomena (Aref *et al.* 2017). For example, solute mixing is singular under chaotic advection (Fereday & Haynes 2004; Cerbelli *et al.* 2017) in that scalar dissipation persists in the limit of vanishingly small molecular diffusivity. Similarly, chaotic advection qualitatively augments both longitudinal (Jones & Young 1994) and transverse dispersion (Lester, Metcalfe & Trefry 2014). Colloidal transport is also strongly augmented by chaotic advection, leading to formation of particle traps, repellers and deposition hot spots on fluid boundaries (Haller & Sapsis 2008; Ouellette, O’Malley & Gollub 2008). Chaotic advection also fundamentally alters chemical reactions (Tél *et al.* 2005; Neufeld & Hernandez-Garcia 2009) and biological activity (Károlyi *et al.* 2000; Tél *et al.* 2000), leading to, e.g. singularly enhanced kinetics, coexistence of competitive species and altered stability characteristics. Hence, detection and quantification of chaotic advection in porous media flows is key to understanding, prediction and upscaling the myriad fluidic processes hosted in porous media.

Chaotic advection is inherent to steady three-dimensional (3-D) pore-scale flow. It is now firmly established (Lester, Metcalfe & Trefry 2013, 2016a; Kree & Villermaux 2017; Turuban *et al.* 2018, 2019; Souzy *et al.* 2020; Heyman, Lester & Le Borgne 2021) that pore-scale chaotic advection arises in almost all porous media, ranging from granular matter to open pore networks. At the Darcy scale, chaotic advection has been predicted or observed in both natural (Trefry *et al.* 2019; Wu *et al.* 2020; Metcalfe *et al.* 2023; Wu *et al.* 2024) and engineered (Metcalfe *et al.* 2010; Mays & Neupauer 2012; Cho *et al.* 2019) transient Darcy flows. However, chaotic advection has not been explicitly detected under steady 3-D Darcy flow, despite consistent observations of complex Lagrangian kinematics (Chiogna *et al.* 2014; Ye *et al.* 2015). Conversely, several recent studies (Lester *et al.* 2021, 2022) have firmly established that chaotic dynamics cannot occur under steady 3-D Darcy

flow with smooth (C^1 -continuous) isotropic hydraulic conductivity fields. As such, the prevalence and nature of chaotic advection in steady heterogeneous Darcy flow is not understood.

In general, chaotic dynamics are to be expected in heterogeneous steady 3-D Darcy flows driven by a constant pressure gradient as these flows share many similarities with steady 3-D duct flows (Speetjens, Metcalfe & Rudman 2021) in that both flow classes comprise a mean axial flow combined with spatially varying transverse flows that can generate chaotic mixing. In the case of duct flows transverse flows are generated by the introduction of static or moving boundary and internal elements, whereas for steady Darcy flow, these transverse flows are generated by heterogeneities in the hydraulic conductivity field. These transverse flows have been shown to generate chaotic advection in a broad set of steady 3-D duct flows (Speetjens *et al.* 2021) ranging from industrial mixing flows (Hobbs & Muzzio 1997; Metcalfe *et al.* 2006; Speetjens, Metcalfe & Rudman 2006) to micro-fluidic devices (Stroock *et al.* 2002; Stone, Stroock & Ajdari 2004; Squires & Quake 2005) and fusion reactors (Boozer 2005) and biological flows (Vétel *et al.* 2009). The parallels between these flow classes indicate that chaotic dynamics should be expected in heterogeneous Darcy flow, however, the finding (Lester *et al.* 2022) that chaotic dynamics cannot occur in some steady 3-D Darcy flows means further investigation is required.

In this study we rigorously establish that chaotic advection is inherent to all steady Darcy flows that are generated by anisotropic and heterogeneous conductivity fields. This is important as many porous media are inherently heterogeneous and anisotropic at the Darcy scale (Bear 1972; Cushman 2013), and solute transport at this scale is typically advection dominated (Bear 1972; Zech *et al.* 2019), hence chaotic advection profoundly impacts solute transport, mixing and reactions. We consider the simplest non-trivial case of steady 3-D Darcy flow arising from a mean potential gradient in an unbounded porous medium with a smooth, finite hydraulic conductivity field. Although this precludes systems with stagnation points, non-smooth conductivity fields or impermeable inclusions, our focus here is to understand basic Darcy flow. To this end, from a conceptual perspective throughout we consider Darcy flow arising from a random (and thus aperiodic) heterogeneous hydraulic conductivity field, but due to computational limitations we perform illustrative calculations on a spatially periodic conductivity field and discuss the implications of such periodicity when interpreting the results of these computations. We establish that chaotic advection arises in the simplest physically plausible heterogeneous conductivity structures, even for weakly heterogeneous porous materials. Conversely, strongly heterogeneous porous media exhibit a Lyapunov exponent close to the theoretical upper bound for steady 3-D flow. We elucidate the underlying mechanisms and establish a quantitative link between the strength of chaotic mixing and (purely advective) transverse dispersion. Application of this link to experimental dispersion data also indicates chaotic mixing is significant and ubiquitous in heterogeneous Darcy flow.

This work is organised as follows. In § 2 we show that all realistic models of heterogeneous media must have anisotropic hydraulic conductivity fields. The braiding of streamlines in Darcy flow and the connection with chaotic advection are then considered in § 3, including development of a quantitative link between transverse dispersion and Lyapunov exponent in random braiding flows. The mechanisms that generate chaotic advection in both periodic and random Darcy flows are considered in § 4. Numerical simulations are performed in § 5, including anisotropic Darcy flow with variable heterogeneity and heterogeneous Darcy flow with varying anisotropy. In § 6 the implications of chaotic advection upon solute mixing, dispersion and reactions are discussed. Conclusions are given in § 7.

2. Kinematics of porous media flows

2.1. Background

We first consider the kinematics of steady 3-D pore-scale flow before upscaling to Darcy flow. Steady 3-D pore-scale flow is described by the Stokes equations

$$\mu \nabla^2 \hat{\mathbf{v}}(\mathbf{x}) - \nabla \hat{p}, \quad \nabla \cdot \hat{\mathbf{v}} = 0, \quad \mathbf{x} \in \Omega_f, \quad (2.1)$$

subject to no-slip conditions $\hat{\mathbf{v}}|_{\partial\Omega_{fs}} = \mathbf{0}$ at the pore boundary $\partial\Omega_{fs}$. Here, μ is the fluid viscosity, $\hat{\mathbf{v}}$ is the pore-scale velocity, \hat{p} the pore-scale pressure field, Ω_f , Ω_s respectively are the fluid (pore) and solid (grain) domains. For steady 3-D flow, the topological complexity of the boundary $\partial\Omega_{fs}$ generates pore-scale chaotic advection (Lester *et al.* 2013). Upscaling by suitable averaging of (2.1) (denoted by $\langle \cdot \rangle_p$) yields the Darcy equation Bear 1972)

$$\mathbf{v}(\mathbf{x}) = -\mathbf{K}(\mathbf{x}) \cdot \nabla \phi(\mathbf{x}), \quad \nabla \cdot \mathbf{v} = 0, \quad \mathbf{x} \in \Omega, \quad (2.2)$$

where $\Omega \equiv \langle \Omega_f \cup \Omega_s \rangle_p$ denotes the Darcy-scale porous medium, $\mathbf{v} \equiv \langle \hat{\mathbf{v}} \rangle_p$ is the (upscaled) Darcy-scale velocity, $\phi \equiv \langle \hat{p} \rangle_p$ the upscaled potential field and $\mathbf{K}(\mathbf{x})$ is the hydraulic conductivity tensor field that captures viscous drag due to no-slip conditions on $\partial\Omega_{fs}$. As this pore boundary generates chaotic advection, omission of $\partial\Omega_{fs}$ in (2.2) via upscaling also omits these pore-scale kinematics. Hence, homogeneous Darcy flow (i.e. $\mathbf{K}(\mathbf{x}) = \text{const.}$) is non-chaotic at the Darcy scale while the pore-scale flow is in general chaotic. At the Darcy scale, the effects of pore-scale chaotic advection must be incorporated via coarse-grained models of e.g. solute mixing (Lester *et al.* 2016b), dispersion (Puyguiraud, Gouze & Dentz 2021) and reaction (Aquino *et al.* 2023). As shall be shown, transverse solute dispersion is especially relevant to understanding chaotic advection in Darcy flow. For solute dispersion, this pore-scale chaotic advection generates mechanical dispersion under pure advection, whereas for diffusive solutes, the interplay of molecular diffusion with pore-scale velocity fluctuations generates hydrodynamic dispersion, which is a function of the pore-scale Péclet number, Pe_p (Bear 1972; Bijeljic & Blunt 2006, 2007; Liu *et al.* 2024), that compares the advection and diffusion time scales over a characteristic pore length. Hydrodynamic dispersion due to pore-scale velocity fluctuations is also referred to as local-scale dispersion. For many applications the pore-scale transverse dispersion coefficient $D_{T,p}$ is assumed to scale with the mean velocity as

$$D_{T,p} = D_m + \alpha_{T,p} ||\mathbf{v}||^n, \quad (2.3)$$

where D_m is molecular diffusivity, $\alpha_{T,p}$ is the pore-scale transverse dispersivity and the empirical index $n \in [1, 2]$ is often taken as unity.

In this study we focus solely on heterogeneous conductivity fields as the majority of porous materials are heterogeneous at the Darcy scale (Bear 1972; Cushman 2013). At scales significantly larger than the largest correlation length scale ℓ of the conductivity field $\mathbf{K}(\mathbf{x})$, the impact of Darcy-scale velocity fluctuations on solute spreading are captured via the macro-dispersion concept (Gelhar & Axness 1983; Dagan 1987).

On the continuum scale, solute transport is typically advection dominated, that is, advection dominates over local-scale dispersion on the correlation scale of hydraulic conductivity. This is measured by the Darcy-scale Péclet number, Pe , which compares the advection and dispersion times over correlation scale ℓ . As shall be shown, the scaling of the transverse macro-dispersion coefficient $D_{T,m}$ with the pore-scale transverse dispersion coefficient $D_{T,p}$ provides important insights regarding the prevalence of chaotic advection in heterogeneous Darcy flow.

For most porous materials the hydraulic conductivity tensor $\mathbf{K}(\mathbf{x})$ is anisotropic due to anisotropy of the underlying pore-scale structure, which occurs in, e.g. stratified formations in geological media and structured engineered media (Bear 1972). Under conventional upscaling approaches the conductivity tensor $\mathbf{K}(\mathbf{x})$ (a second rank tensor) is symmetric and positive definite (Bear 1972), with six independent components in 3-D space which vary spatially in heterogeneous formations but are all assumed to be smooth, continuous and finite. In the absence of boundaries and fluid sources and sinks, the positive-definite nature of $\mathbf{K}(\mathbf{x})$ renders Darcy-scale flow stagnation free, i.e. $\mathbf{v}(\mathbf{x}) \neq \mathbf{0} \forall \mathbf{x} \in \Omega$ (Bear 1972). As $\mathbf{K}(\mathbf{x})$ is symmetric, it may be locally diagonalised into principal directions with three independent components as $\mathbf{K}'(\mathbf{x}) = \mathbf{R}(\mathbf{x}) \cdot \mathbf{K}(\mathbf{x}) \cdot \mathbf{R}^{-1}(\mathbf{x})$, where $\mathbf{R}(\mathbf{x})$ is a rotation tensor field and

$$\mathbf{K}'(\mathbf{x}) \equiv \begin{pmatrix} K'_{11}(\mathbf{x}) & 0 & 0 \\ 0 & K'_{22}(\mathbf{x}) & 0 \\ 0 & 0 & K'_{33}(\mathbf{x}) \end{pmatrix}. \quad (2.4)$$

Even if $\mathbf{R}(\mathbf{x})$ is spatially invariant, this conductivity field is fundamentally anisotropic if one of the diagonal components $K'_{ii}(\mathbf{x})$ differs from the others.

Conversely, many studies (Gelhar & Axness 1983; Neuman & Zhang 1990; Chaudhuri & Sekhar 2005; Delgado 2007; Janković *et al.* 2009; Beaudoin & de Dreuzy 2013; Boon *et al.* 2016; Dartois, Beaudoin & Huberson 2018) consider the hydraulic conductivity tensor to be isotropic as $\mathbf{K}(\mathbf{x}) = k(\mathbf{x})\mathbf{I}$, where $k(\mathbf{x}) = K'_{ii}(\mathbf{x})$ for $i = 1 : 3$, and (2.2) simplifies to

$$\mathbf{v}(\mathbf{x}) = -k(\mathbf{x})\nabla\phi, \quad \nabla \cdot \mathbf{v} = 0, \quad \mathbf{x} \in \Omega. \quad (2.5)$$

The kinematics of isotropic Darcy flow markedly differ from that of anisotropic Darcy flow. If $k(\mathbf{x})$ is smooth and \mathbf{v} does not admit stagnation points, then isotropic Darcy flow only admits simple kinematics because the helicity density $\mathcal{H}(\mathbf{x}) \equiv \mathbf{v} \cdot (\nabla \times \mathbf{v})$ is identically zero

$$\mathcal{H}(\mathbf{x}) = k\nabla\phi \cdot (\nabla\phi \times \nabla k) = 0, \quad (2.6)$$

regardless of the heterogeneity of $k(\mathbf{x})$. For inviscid flows, the total helicity $H \equiv \int_{\Omega} \mathcal{H}(\mathbf{x}) \, \mathrm{d}\mathbf{x}$ over the flow domain Ω is a topological invariant that characterises the topological complexity (knottedness) of vortex lines of the flow (Woltjer 1958; Moreau 1961; Moffatt 1969), but in general the zero helicity density condition $\mathcal{H}(\mathbf{x}) = 0$ precludes chaotic dynamics in steady 3-D flows (Arnol'd 1965; Moffatt & Tsinober 1992). Hence steady 3-D isotropic Darcy flows are non-chaotic and integrable and so admit two invariants ψ_1, ψ_2 that act as streamfunctions (Yoshida 2009; Lester *et al.* 2022), leading to the Euler velocity representation

$$\mathbf{v}(\mathbf{x}) = \nabla\psi_1(\mathbf{x}) \times \nabla\psi_2(\mathbf{x}). \quad (2.7)$$

Streamlines of steady isotropic Darcy flow are confined to the intersections of streamsurfaces given by level sets of $\psi_1(\mathbf{x}), \psi_2(\mathbf{x})$. Such confinement prohibits transverse macro-dispersion (henceforth simply termed transverse dispersion) of the streamlines of \mathbf{v} in the absence of local-scale dispersion, regardless of medium heterogeneity (Lester *et al.* 2023).

2.2. Implications for hydraulic conductivity modelling

These kinematic constraints are illustrated in figure 1(c), which shows typical streamlines for isotropic Darcy flow generated by a strongly heterogeneous ($\sigma_{\ln K}^2 = 4$) hydraulic conductivity field. Although the streamlines are highly tortuous due to heterogeneity of

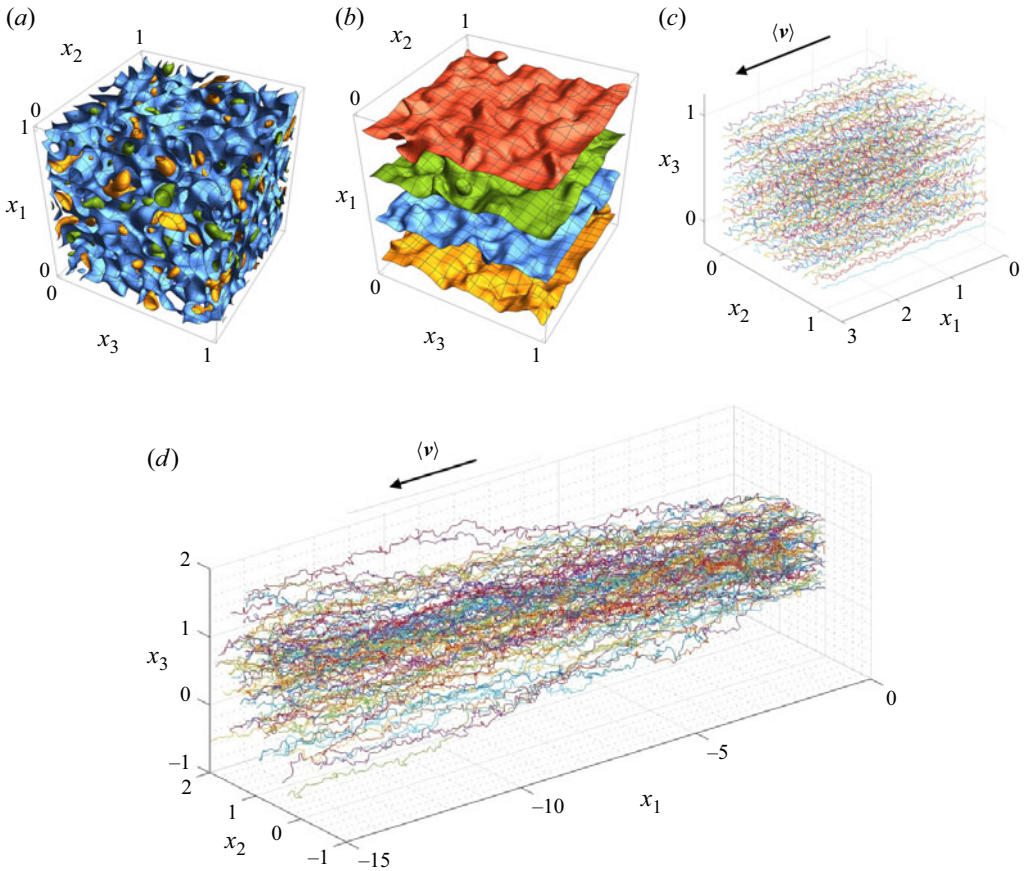


Figure 1. (a) Isosurfaces of the typical normalised heterogeneous log-conductivity field $f(\mathbf{x}) = \ln K(\mathbf{x})/\sigma_{\ln K}^2$ used to model isotropic $k(\mathbf{x})\mathbf{I}$ and anisotropic $\mathbf{K}(\mathbf{x})$ conductivity tensors and (b) associated potential field $\phi(\mathbf{x})$ for anisotropic Darcy flow driven by a uniform mean potential gradient. Note coloured surfaces are isopotential surfaces $\phi = \text{const}$. Associated streamlines for heterogeneous Darcy flow with (c) isotropic conductivity field ($\delta = 0$ in (5.1)) and (d) anisotropic conductivity field ($\delta = 1$ in (5.1)) with log-conductivity variance $\sigma_{\ln K}^2 = 4$ and parameters $N = 4$, $N_i = 2$ in (5.2).

the medium, they do not exhibit asymptotic transverse dispersion. In § 5.1 the transverse dispersivity of this flow is numerically computed to be effectively zero.

These kinematic constraints persist even if the scalar field $k(\mathbf{x})$ is statistically anisotropic (i.e. has different correlation structures in different principal directions), as the corresponding Darcy flow is still locally isotropic and $\mathcal{H}(\mathbf{x}) = 0$. We remark on the application of these results to the so-called ‘helicity paradox’ (Cirpka *et al.* 2015) that occurs when a statistically anisotropic but locally isotropic conductivity field is upscaled from the Darcy scale to the block field scale, resulting in an anisotropic block-scale conductivity field (Bear 1972). This spuriously adds degrees of freedom to the Lagrangian kinematics and permits block-scale chaotic advection where none should exist based on the fully resolved Darcy-scale flow. While beyond the scope of this paper, our results highlight the need for upscaling methods that obey the appropriate kinematic constraints.

These results provide insights into the connection between transverse macro-dispersion in steady Darcy flow and anisotropy of the hydraulic conductivity tensor $\mathbf{K}(\mathbf{x})$. Unfortunately, the prevalence (or otherwise) of transverse macro-dispersion in field studies

is an open question. While recent analyses (Zech *et al.* 2019) of field experiments of solute transport (Sudicky, Cherry & Frind 1983; Rajaram & Gelhar 1991; Hess, Wolf & Celia 1992) over a range of geological media clearly establish that longitudinal macro-dispersivity is significantly greater than pore-scale dispersivity, indicating the presence of large-scale conductivity heterogeneities at the Darcy scale, similar data are inconclusive with respect to transverse dispersivity. Hence, the prevalence of transverse macro-dispersion in groundwater flows in heterogeneous aquifers is currently unknown.

Although several numerical studies (Janković *et al.* 2009; Beaudoin & de Dreuzy 2013; Dartois *et al.* 2018) have found that isotropic Darcy flow can generate purely advective transverse dispersion, these observations arise in systems with either non-smooth conductivity fields or impermeable inclusions, or from numerical schemes that violate the kinematic constraints associated with (2.7). Similar to how integration schemes that are not symplectic violate Hamiltonian constraints (i.e. invariance of the Hamiltonian), numerical schemes that are not explicitly designed to do so also violate the constraints associated with (2.7). Lester *et al.* (2023) show that numerical schemes that implicitly enforce these constraints yield zero transverse dispersivity.

Conversely, anisotropic conductivity fields $\mathbf{K}(\mathbf{x})$ generate non-zero helicity density

$$\mathcal{H}(\mathbf{x}) = (\mathbf{K} \cdot \nabla \phi) \cdot (\nabla \times \mathbf{K} \cdot \nabla \phi) \neq 0, \quad (2.8)$$

and non-zero total helicity $H \neq 0$. Hence, the streamlines of anisotropic Darcy flow are no longer constrained to the streamsurfaces of $\psi_1(\mathbf{x})$, $\psi_2(\mathbf{x})$, but rather freely wander through the medium (Lester *et al.* 2023), giving rise to persistent transverse dispersion. This behaviour is shown in figure 1(d), where the streamlines associated with strongly heterogeneous ($\sigma_{lnK}^2 = 4$) anisotropic Darcy flow spread transversely throughout the flow domain as they are advected longitudinally. In § 5.1 the transverse dispersion coefficient D_T of this flow is quantitatively shown to be non-zero.

Note that non-zero helicity density $\mathcal{H}(\mathbf{x}) \neq 0$ alone is not sufficient to ensure non-zero transverse dispersivity. Yoshida (2009) shows that only 3-D velocity fields given by the complete Clebsch parameterisation

$$\mathbf{v}(\mathbf{x}) = \sum_{i=1}^{N=2} \alpha_i(\mathbf{x}) \nabla \beta_i(\mathbf{x}) + \nabla \varphi(\mathbf{x}), \quad (2.9)$$

where $\alpha_i(\mathbf{x})$, $\beta_i(\mathbf{x})$, $\varphi(\mathbf{x})$ are smooth continuous scalar fields, have non-zero total helicity H and so admit chaotic advection. Conversely, the classical Clebsch parameterisation

$$\mathbf{v}(\mathbf{x}) = \alpha_1(\mathbf{x}) \nabla \beta_1(\mathbf{x}) + \nabla \varphi(\mathbf{x}) \quad \mathbf{x} \in \Omega, \quad (2.10)$$

has been found to be incomplete (Yoshida 2009), meaning that some 3-D vector fields cannot be represented by (2.10). Yoshida & Morrison (2017) classify flows conforming to (2.10) as epi-2-D flows which are topologically two-dimensional with non-zero helicity density $\mathcal{H}(\mathbf{x}) = \nabla \varphi_1 \cdot (\nabla \alpha_1 \times \nabla \beta_1) \neq 0$ but are helicity free, with $H = 0$. Conversely, realistic heterogeneous conductivity models yield 3-D velocity fields of the form (2.9) that admit chaotic advection and transverse dispersion.

To summarise, if transverse macro-dispersion is non-zero in heterogeneous aquifers in the advection-dominated limit, that is, in the absence of local-scale dispersion, then hydraulic conductivity models of heterogeneous porous media must be anisotropic to be consistent. Although the prevalence of transverse macro-dispersion in field studies is inconclusive, we note that many aquifers have an anisotropic geological structure and many groundwater models utilise anisotropic hydraulic conductivity fields to predict solute transport in groundwater applications. As non-zero transverse macro-dispersion requires

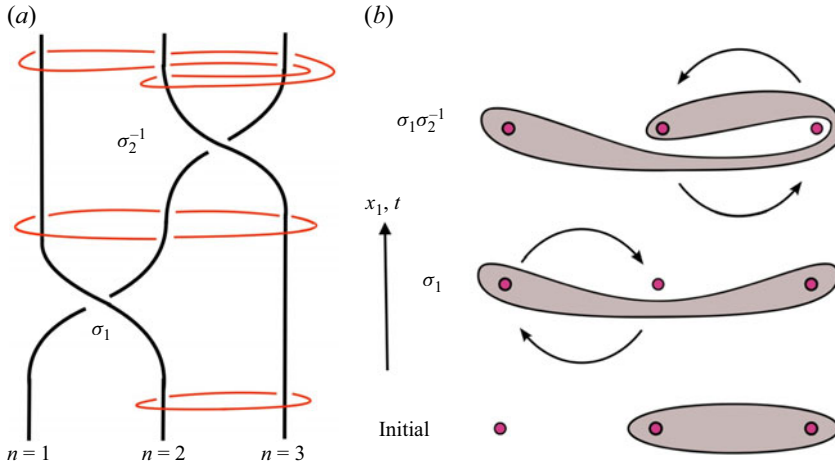


Figure 2. (a) Braid diagram depicting stretching of material elements (red) around fluid particle streamlines (black) numbered $n = 1$ to $n = 3$ from left to right in a 3-dof flow. For a steady 3-D flow braiding evolves in the longitudinal x_1 coordinate, and for an unsteady 2-D flow braiding evolves with respect to time t . The pathline crossing events are characterised by the respective braid generators σ_1 and σ_2^{-1} , which act to stretch the material element due to the topology of the braiding motions. (b) Stretching of material elements (brown) due to braiding motions (adapted from Thiffeault 2022) of streamlines (red circles) corresponding to the braid diagram in (a) that evolves with the longitudinal direction x_1 or time t .

$H \neq 0$, this raises the potential for chaotic advection, which is inevitable in nonlinear continuous systems with arbitrary coefficients and three degrees of freedom (dof = 3) (Speetjens *et al.* 2021). In the following section we firmly establish that transverse macro-dispersion and chaotic advection are intimately linked in Darcy flow.

3. Streamline braiding and chaos

3.1. Background

The link between dispersion and chaotic mixing can be explored via consideration of streamline braiding. As 1-D streamlines are invariants of steady 3-D flow, braiding of streamlines stirs fluid elements in a complex manner, as illustrated in figure 2. This concept has been used to quantify stirring in another 3-dof system – unsteady 2-D flow – where non-trivial braiding of 1-D pathlines can also stretch and fold the fluid continuum. For unsteady 2-D flow, braid group theory (Handel & Thurston 1985; Boyland, Aref & Stremler 2000; Moussafer 2006) has been developed to quantify the topological entropy h_{braid} of the pathline braiding motions, closely related to the Lyapunov exponent λ_∞ (Thiffeault 2005). In § 3.2 we show that steady 3-D Darcy flow is topologically equivalent to 2-D unsteady flow, hence this mathematical framework applies to these flows.

The topological equivalence between stagnation-free steady 3-D flow and unsteady 2-D flow has been established since the earliest studies of chaotic advection (Aref 1984; Bajer 1994), with particular focus on steady 3-D duct flows (Lester *et al.* 2018b; Speetjens *et al.* 2021). Steady heterogeneous 3-D Darcy flow driven by a unidirectional mean pressure gradient shares many similarities with stagnation-free steady 3-D duct flows in that both flows are topologically equivalent to unsteady 2-D flow and chaotic advection arises due to transverse perturbations away from a fully integrable state. However, a fundamental difference between these flows is that heterogeneous Darcy flow is typically random and aperiodic, meaning the tools and techniques of Hamiltonian chaos for temporally periodic

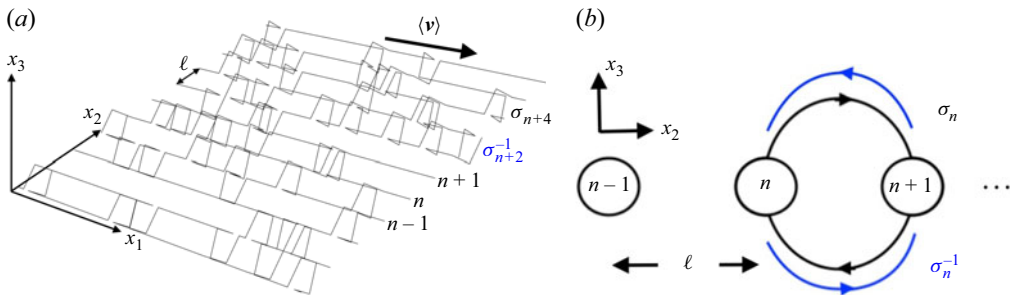


Figure 3. (a) Propagation of 1-D streamlines (black) in a steady unidirectional 3-D flow with mean flow in the longitudinal (x_1) direction. (b) Schematic of braiding of streamlines (black circles) labelled $n-1$, n , $n+1$ in the transverse $x_2 - x_3$ plane via clockwise (black) σ_n , anti-clockwise (blue) σ_n^{-1} braid generators.

2-D systems (Poincaré sections, analysis of periodic points, resolution of hyperbolic manifolds and Kolmogorov–Arnold–Moser islands) (Ottino 1989) do not apply to these flows. While tools such as Lagrangian coherent structures (LCS) (Haller 2015) are well suited to uncover the advection structure of aperiodic flows, in this study we focus on braid group theory (or topological fluid mechanics) (Boyland *et al.* 2000) as this approach, as shall be shown, provides a vital quantitative link between chaotic advection and transverse dispersion that is central to this study.

Braid group theory is used to quantify stirring in unsteady 2-D flows (Boyland *et al.* 2000) via a well-developed mathematical framework (Artin 1947; Moussafir 2006; Thiffeault 2022) that efficiently encodes fluid stirring via a symbolic braiding representation of the topology of pathlines in space–time. This encoding can be used to compute the topological complexity of their braiding motions, and the Neilson–Thurston classification theorem (Handel & Thurston 1985) characterises braids as periodic, reducible or pseudo-Anosov types, the latter of which is interpreted as an indicator of chaotic dynamics (Boyland *et al.* 2000). Due to topological equivalence, this framework can also be applied to streamline braiding in steady 3-D Darcy flow.

For steady unidirectional 3-D flow, streamline braiding is encoded via a sequence of braid generators $\sigma_n^{\pm 1}$ (Artin 1947). Figure 3(a) shows propagation in the x_1 direction of a set of streamlines of a steady unidirectional 3-D flow that undergo random ‘crossing’ motions with respect to the transverse x_3 coordinate. As shown in figure 3(b), these crossing motions can be characterised in terms of the braid generators σ_n and σ_n^{-1} , which respectively characterise clockwise and counter-clockwise crossing of streamlines n and $n+1$ in the transverse (x_2, x_3) plane. Note streamlines are labelled $(\dots, n-1, n, n+1, \dots)$ with respect to their relative position in the x_2 coordinate, so these labels are updated after each crossing event. An ordered sequence of braid generators forms the braid word $\mathbf{b} = \sigma_{n_1}^{\pm 1} \sigma_{n_2}^{\pm 1} \dots$, which is determined by the sequence of streamline crossings in the x_1 direction. Hence, \mathbf{b} completely characterises the topological braiding motions of the streamlines. As shown in figure 2(b), these braiding motions act to stretch and fold fluid elements (brown), leading to exponential stretching if they are of pseudo-Anosov type.

The rate of stretching generated by a braid word \mathbf{b} is given by its topological braid entropy h_{braid} . In general, the topological entropy \hat{h} of a dynamical system measures the rate of loss of information of the system about its initial conditions. For fluid flows \hat{h} is closely related to the largest infinite-time Lyapunov exponent $\hat{\lambda}_{\infty}$ and forms an upper bound for $\hat{\lambda}_{\infty}$ (Thiffeault 2010). In practice, the topological entropy of a flow can be interpreted as the asymptotic exponential growth rate of the length $l(t)$ of a material line

(Newhouse & Pignataro 1993) as

$$\hat{h} = \lim_{t \rightarrow \infty} \frac{1}{t} \ln \frac{l(t)}{l(0)}. \quad (3.1)$$

For ergodic flows such as purely hyperbolic steady 3-D flow (which has a single positive Lyapunov exponent and does not admit non-hyperbolic features such as elliptic or parabolic LCS (Haller 2015)), the upper bound given by the topological entropy is exact (Yomdin 1987; Newhouse 1988; Newhouse & Pignataro 1993; Matsuoka & Hiraide 2015; Catalan 2019), i.e.

$$\hat{h} = \hat{\lambda}_{\infty}. \quad (3.2)$$

Conversely, many studies dating over half a century (Cocke 1969; Girimaji & Pope 1990; Hinch 1999; Kalda 2000; Duplat, Innocenti & Villiermaux 2010; Villiermaux 2019) propose that as fluid elements undergo stretching, the relative length $\rho \equiv \delta l(t)/\delta l(0)$ of infinitesimal line elements is distributed log normally with log mean $\hat{\lambda}_{\infty} t$ and log variance $\hat{\sigma}_{\lambda}^2 t$. In § 5.2 and Appendix C we confirm that an *ab initio* derivation of fluid stretching in steady 3-D flows yields the same result if the velocity distribution does not yield anomalous transport. For this scenario a reasonable conclusion (Hinch 1999; Duplat *et al.* 2010; Villiermaux 2019) is that the growth rate of a material line of length $l(t) = \int_0^{l(0)} \delta l(X, t) dX$ (where X is the Lagrangian coordinate along the line) is given by the ensemble average of ρ , which, via (3.1), yields

$$\hat{h} = \hat{\lambda}_{\infty} + \frac{\sigma_{\lambda}^2}{2}, \quad (3.3)$$

as the variance of $\ln \rho$ contributes to the growth of $\ln l(t)$. However, the discrepancy between (3.3) and (3.2) has recently been explained by Lester & Dentz (2025), who show that in the asymptotic limit, temporal sampling of the finite-time Lyapunov exponent $\hat{\lambda}(X, t)$ (which converges to $\hat{\lambda}_{\infty}$ as $\sigma_{\lambda}/\sqrt{t}$) dominates over the ensemble average represented by (3.3), yielding (3.2). In § 4 we show that heterogeneous Darcy flow with random stationary conductivity $\mathbf{K}(\mathbf{x})$ is ergodic and purely hyperbolic.

The dimensionless topological entropy $h \equiv \hat{h}\ell/\langle v_1 \rangle$ (with velocity correlation length ℓ) may be approximated by considering the topological braid entropy h_{braid} of the braid word \mathbf{b} comprising a set of N_b braiding motions of N_p streamlines of the flow (Thiffeault 2010). The braid entropy h_{braid} characterises the asymptotic growth of the number of distinguishable orbits of the braid (Thiffeault 2022). For steady 3-D flow this may be interpreted as the number of distinct linkages that a material line makes if it is fully contracted until it forms a loop ℓ_E that tightly contacts these streamlines, where the metric $|\ell_E|$ measures the number of linkages of the loop ℓ_E . For example, the evolving brown material element shown in figure 2(b) can be approximated as a number of straight linkages that either connect to or touch the red stirring rods. Under the initial configuration, the element can be approximated as one linkage ($|\ell_E| = 1$) connecting the $n = 2$ and $n = 3$ rods, but after the braid generator σ_1 , there are two linkages ($|\ell_E| = 2$) connecting the $n = 1$ to $n = 2$ to $n = 3$ rods, and finally after $\sigma_1 \sigma_2^{-1}$ there are three linkages ($|\ell_E| = 3$) connecting rods $n = 1$ to $n = 2$, $n = 2$ to $n = 3$ and then $n = 3$ to $n = 2$. The topological entropy h_{braid} of a braid word \mathbf{b} is then

$$h_{\text{braid}} = \lim_{k \rightarrow \infty} \frac{1}{k} \log \frac{|\mathbf{b}^k \ell_E|}{|\ell_E|}, \quad (3.4)$$

where $\mathbf{b}^k \ell_E$ indicates the braid \mathbf{b} has operated k times on the loop ℓ_E . Although non-trivial, various methods (Moussafir 2006; Hall & Yurttas 2009; Thiffeault 2022) are available to rigorously compute h_{braid} from a given braid word \mathbf{b} . As the braid entropy h_{braid} only considers the complexity of streamline braiding, it forms a lower bound for h , however, for many systems it converges to h with increasing number of streamlines N_p and braiding motions N_b as

$$\lim_{N_p \rightarrow \infty} \lim_{N_b \rightarrow \infty} \frac{h_{\text{braid}}}{t} \rightarrow \hat{h} = \hat{\lambda}_{\infty}. \quad (3.5)$$

Hence, for heterogeneous Darcy flow both the topological entropy h and dimensionless Lyapunov exponent $\lambda_{\infty} \equiv \hat{\lambda}_{\infty} \ell / \langle v_1 \rangle$ may be accurately estimated from the braid entropy h_{braid} of a sufficiently resolved set of streamlines (large N_p) recorded over a sufficient observation time (large N_b).

3.2. Topology of steady heterogeneous 3-D Darcy flow

The topology of steady 3-D flows $\mathbf{v}(\mathbf{x}) = [v_1(\mathbf{x}), v_2(\mathbf{x}), v_3(\mathbf{x})]$ with one unidirectional (axial) velocity component (e.g. $v_1(\mathbf{x}) > 0$) can be equated (Bajer 1994) to that of unsteady 2-D flow via the rescaling $\mathbf{v}'(\mathbf{x}) = \mathbf{v}(\mathbf{x})/v_1(\mathbf{x})$, $t' = x_1$, such that the x_1 coordinate acts as an analogue for time t , hence the advection equation transforms as

$$\frac{d}{dt}[x_1, x_2, x_3]^{\top} = [v_1, v_2, v_3]^{\top} \Rightarrow \frac{d}{dt'}[x_2, x_3]^{\top} = \left[\frac{v_2(t', x_2, x_3)}{v_1(t', x_2, x_3)}, \frac{v_3(t', x_2, x_3)}{v_1(t', x_2, x_3)} \right]^{\top}. \quad (3.6)$$

This transformation brings several advantages with respect to analysis of the advective mixing properties of the flow, as axially periodic 3-D flows such as duct flows (Speetjens *et al.* 2021) can be couched as temporally periodic 2-D flows, hence the tools and techniques of Hamiltonian chaos (Aref 1984; Ottino 1989) can be used to study mixing in these systems. Although the analogous 2-D flow in (3.6) is no longer divergence free, the dynamics of this flow is still Hamiltonian in the stroboscopic frame (Bajer 1994). For aperiodic 3-D duct flows, conversion to aperiodic transient 2-D flows via (3.6) facilitates the use of tools such as LCS (Haller 2015) to uncover the mixing dynamics of these flows. Indeed, this transformation has been used to study a wide class of both periodic and aperiodic steady 3-D duct flows (Speetjens *et al.* 2006).

For strongly heterogeneous 3-D Darcy flows the transformation (3.6) breaks down when $v_1(\mathbf{x})$ is zero (Bajer 1994) due to flow reversal in the vicinity of low permeability structures. However, these flows are still fundamentally unidirectional as the potential field $\phi(\mathbf{x})$ is strictly monotonic decreasing along streamlines $\nabla \phi(\mathbf{x}) \cdot \mathbf{v}(\mathbf{x}) = -\nabla \phi(\mathbf{x}) \times \mathbf{K}(\mathbf{x}) \cdot \nabla \phi(\mathbf{x}) < 0$ due to the positive definite nature of $\mathbf{K}(\mathbf{x})$ (Bear 1972). This leads to the intrinsic coordinate basis $\xi = (\chi_1, \chi_2, \phi)$, where χ_1, χ_2 are arbitrary coordinates which are both orthogonal to ϕ , and the intrinsic velocity representation $\mathbf{v}_{\xi}(\xi) = [v_{\chi_1}(\xi), v_{\chi_2}(\xi), v_{\phi}(\xi)]$ with $v_{\phi}(\xi) > 0$. Thus, the intrinsic velocity field $\mathbf{v}_{\xi}(\xi)$ may be rescaled as

$$\mathbf{v}'_{\xi}(\xi) = \left[\frac{v_{\chi_1}(\xi)}{v_{\phi}(\xi)}, \frac{v_{\chi_2}(\xi)}{v_{\phi}(\xi)}, 1 \right], \quad v_{\phi}(\xi) > 0 \forall \xi \in \Omega. \quad (3.7)$$

This velocity field is topologically equivalent to that of unsteady 2-D flow, and the isopotential surfaces of steady 3-D Darcy flow (figure 1b) are analogous to isochrones of unsteady 2-D flow. This means that steady 3-D Darcy flow always has an embedded Hamiltonian structure (and associated Lagrangian kinematics) as explained in §4.3 of

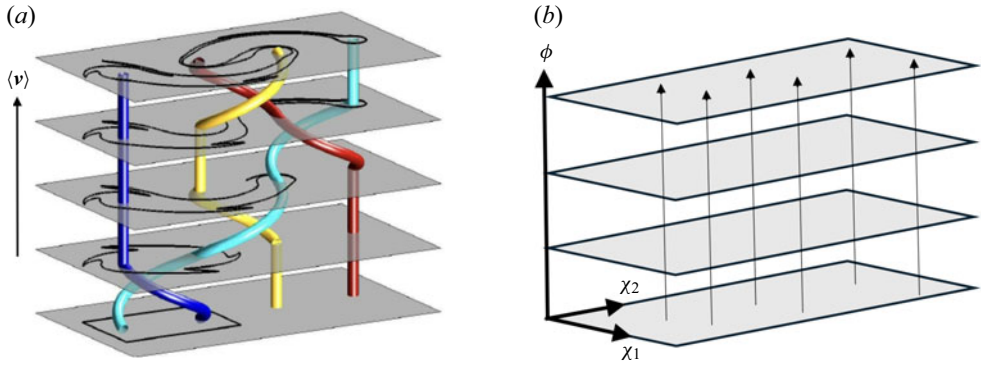


Figure 4. (a) Schematic of streamline (or pathline) braiding in a unidirectional steady 3-D flow (or unsteady 2-D flow). The set of four thick coloured streamlines (or pathlines) braid with each other as they evolve with the mean flow direction x_3 (or time t). This topological braiding motion stirs the fluid continuum (grey planes) and the length of the black rectangular material boundary grows exponentially with the number of braiding motions. Adapted from Thiffeault & Finn (2006). This schematic also depicts streamline braiding in steady 3-D anisotropic Darcy flow with intrinsic coordinates $\xi = (\chi_1, \chi_2, \phi)$, where the grey planes depict isopotential surfaces. (b) Absence of braiding in isotropic Darcy flow in intrinsic coordinates $\xi = (\chi_1, \chi_2, \phi)$. As the velocity field is everywhere orthogonal to level sets of ϕ denoted by grey planes, streamlines in this coordinate system (which are simply straight lines) do not move laterally or undergo braiding.

Speetjens *et al.* (2021), and so maintains a fundamental connection with the generation of chaotic advection in stagnation-free steady 3-D flows in general.

As such, streamlines in steady 3-D Darcy flow are topologically equivalent to pathlines of unsteady 2-D flow and the mathematical framework developed for pathline braiding can be directly applied to steady 3-D Darcy flow. As per figure 4(b), the representation (3.7) also shows directly that isotropic Darcy flow cannot generate streamline braiding, where $(\chi_1, \chi_2) = (\psi_1, \psi_2)$ and (3.7) simplifies to $\mathbf{v}'_\xi(\xi) = (0, 0, 1)$ because the velocity field is everywhere orthogonal to the level sets of ϕ , i.e. $\mathbf{v} \times \nabla\phi = \mathbf{0}$. These streamlines do not move relative to each other in the isopotential surfaces $\phi = \text{const.}$, let alone undergo non-trivial braiding motions. In Cartesian coordinates (figure 1c), the helicity-free condition constrains non-braiding yet tortuous streamlines to streamsurfaces $\psi_1(\mathbf{x}) = \text{const.}$, $\psi_2(\mathbf{x}) = \text{const.}$ Conversely, anisotropic Darcy flow admits non-zero transverse velocity components $v_{\chi_1}(\xi)$, $v_{\chi_2}(\xi)$ and so streamlines can undergo the braiding motions as shown in figures 4(a) and 1(d). Although transverse motion of streamlines in the (χ_1, χ_2) directions does not necessarily generate non-trivial braiding, below we show that non-trivial braiding is inherent to steady random 3-D flows.

3.3. Linking dispersion and chaos in streamline braiding flows

Lester, Metcalfe & Trefry (2024) recently examined the link between chaotic advection and transverse dispersion in randomly braiding flows via a simple 1-D streamline model. As per figure 3(a), this model consists of a set of N_p streamlines in \mathbb{R}^3 space that repeat periodically in the transverse x_2 direction and propagate due to mean flow in the longitudinal x_1 direction. These streamlines have the same x_3 -coordinate ($x_3 = 0$) and uniform spacing $\Delta x_2 = \ell$ in the x_2 -direction, corresponding to the velocity correlation length scale ℓ . At integer multiples of longitudinal distance Δ_L/N_p , one pair $(n, n+1)$ of neighbouring streamlines randomly exchange position in the $x_2 - x_3$ plane via clockwise or counter-clockwise rotations, as labelled by the respective braid generators σ_n, σ_n^{-1} . Figure 5(a) shows the braid diagram for a typical braid word \mathbf{b} consisting of $N_p = 20$

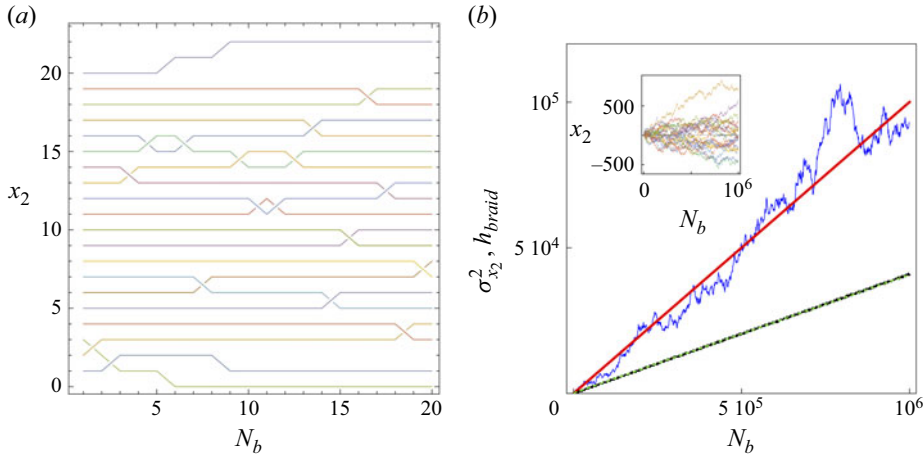


Figure 5. (a) Braid diagram for 1-D streamline depicting evolution of x_2 coordinate of $N_p = 20$ streamlines over $N_b = 20$ random braid actions in the longitudinal x_1 direction, leading to non-trivial braiding and dispersion of streamlines. (b) Linear growth of topological braid entropy h_{braid} (black points) with N_b , in agreement with (3.13) (green dashed line). Growth of transverse variance $\sigma_{x_2}^2(N_b)$ (blue line) with N_b , in agreement with (3.11) (red line). Inset: Brownian motion of pathlines with increasing N_b .

streamlines and $N_b = 20$ braid generators. For an array of N_p streamlines, the distance Δ_L/N_p corresponds to a braid frequency \hat{f} per streamline of

$$\hat{f} \equiv \frac{\langle v_1 \rangle}{\Delta_L}. \quad (3.8)$$

The streamline braiding motions are defined by a braid word \mathbf{b} comprising N_b braid generators $\mathbf{b} = \sigma_{n_1}^{\pm 1} \sigma_{n_2}^{\pm 1} \dots \sigma_{n_{N_b}}^{\pm 1}$ which is constructed by randomly choosing each generator from the set $\{\sigma_1, \sigma_1^{-1}, \dots, \sigma_{N_p}, \sigma_{N_p}^{-1}\}$. Note that, due to periodicity, the $n = N_p$ pathline can braid with the $n = 1$ pathline via the σ_{N_p} and $\sigma_{N_p}^{-1}$ braid generators as an annular braid (Finn & Thiffeault 2007). Hence, streamlines undertake an unbounded random walk along the x_2 coordinate as they propagate longitudinally (figure 5b, inset), while deforming the interstitial fluid as per figure 2. The topological braid entropy h_{braid} of these motions is efficiently computed via the *braidlab* package (Thiffeault & Budišić 2013–2021). Figure 5(b) shows linear growth of topological braid entropy h_{braid} and transverse variance $\sigma_{x_2}^2$ of this system with N_b .

Lester *et al.* (2024) show that the topological braid entropy h_{braid} and transverse variance $\sigma_{x_2}^2$ of this system grow linearly with N_b , and in the limit of large N_b and N_p , the scaled mean topological braid entropy $\langle h_{braid} \rangle$ for 10^3 realisations of this simple 1-D streamline model converges to the random braid entropy $\langle \lambda_\sigma \rangle$ as

$$\lim_{N_p \rightarrow \infty} \lim_{N_b \rightarrow \infty} \frac{N_p}{N_b} \langle h_{braid} \rangle \rightarrow \frac{\Delta_L}{\langle v_1 \rangle} \hat{h} \equiv \langle \lambda_\sigma \rangle = 0.8529. \quad (3.9)$$

The random braid entropy $\langle \lambda_\sigma \rangle$ is a fundamental quantity in that it characterises the topological entropy of random braids in limit of large N_p and N_b . From (3.9), the random braid entropy is related to the dimensionless Lyapunov exponent λ_∞ and topological entropy h as

$$\lambda_\infty = h = \frac{\ell}{\Delta_L} \langle \lambda_\sigma \rangle = f \langle \lambda_\sigma \rangle, \quad (3.10)$$

where $f \equiv \hat{f}\ell/\langle v_1 \rangle$ is the dimensionless braiding frequency that characterises the frequency of braiding events for a single streamline. As $\langle \lambda_\sigma \rangle$ is a universal constant, f is necessary and sufficient to completely characterise streamline braiding in random braiding flows. For streamlines with mean spacing ℓ , f characterises the average longitudinal distance Δ_L between braiding events in steady 3-D flow. Together, $\langle \lambda_\sigma \rangle$ and f quantify the topological entropy h of the 1-D streamline model shown in [figure 3\(a\)](#).

These quantities can also be connected to the advective transverse dispersion coefficient D_T driving the growth of $\sigma_{x_2}^2$ shown in [figure 5\(b\)](#). As two of the N_p streamlines make random jumps in the x_2 direction of $\pm\ell$ with each braiding event, the spatial variance $\sigma_{x_2}^2$ of streamlines grows linearly with N_b as

$$\sigma_{x_2}^2(t) = \sigma_{x_2}^2(0) + 2\ell^2 \frac{N_b}{N_p} \equiv \sigma_{x_2}^2(0) + 2D_T t, \quad (3.11)$$

where the variance growth per braid event is $2\ell^2/N_p$ as each event moves two of the N_p streamlines by $\pm\ell$. As $N_b = N_p \langle v_1 \rangle t / \Delta_L$, then

$$D_T = \frac{\ell^2 \langle v_1 \rangle}{\Delta_L}, \quad (3.12)$$

which, as shown in [figure 5\(b\)](#), agrees well with model observations. Defining the advective transverse Péclet number as $Pe_T \equiv D_T / (\langle v_1 \rangle \ell)$ then yields $Pe_T = 1/f$. Hence, for the 1-D streamline model the dimensionless Lyapunov exponent λ_∞ and topological entropy h are linearly related to the transverse dispersion coefficient D_T as

$$\lambda_\infty = h = \frac{\langle \lambda_\sigma \rangle}{Pe_T} = f \langle \lambda_\sigma \rangle. \quad (3.13)$$

This linear relationship arises as the 1-D streamline model generates transverse dispersion and chaotic advection in equal measure.

Two different 2-D extensions of this 1-D streamline model were also considered by Lester *et al.* (2024); one involving a 2-D streamline array analogous to the 1-D array in [figure 5\(a\)](#), and another involving 3-D streamlines that undertake independent random walks constructed by making a jump of fixed magnitude by random orientation in the $x_2 - x_3$ plane at regular intervals in the x_1 coordinate. For both of these models the appropriately scaled topological braid entropy h_{braid} was also found to converge to the random braid entropy $\langle \lambda_\sigma \rangle$, leading to a simple relationship between the Lyapunov exponent λ_∞ of the flow and the transverse Péclet number Pe_T as

$$h = \lambda_\infty = f^{1/d} \langle \lambda_\sigma \rangle = \left(\frac{d}{Pe_T} \right)^{1/d} \langle \lambda_\sigma \rangle, \quad d = 1, 2, \quad (3.14)$$

which generalises (3.13) to $d = 1$ or $d = 2$ dimensional streamline arrays. The persistence of this relationship across these diverse models suggests that they all belong to the same universality class (Ódor 2004) associated with streamline braiding. This establishes that chaotic advection and transverse dispersion are intimately linked in heterogeneous Darcy flow because they are both driven by non-trivial streamline braiding. Equation (3.14) also points to development of methods to estimate λ_∞ from transverse dispersivity data for specific systems; however, further research is required to extend this link to non-ideal systems.

3.4. Fluid deformation in heterogeneous Darcy flow

In addition to streamline braiding, it is also instructive to consider *ab initio* evolution of fluid deformation in heterogeneous Darcy flow from a kinematic perspective. This can be quantified by considering deformation as a random process. Le Borgne *et al.* (2008a,b) established that for steady flow in random media, the velocity magnitude v decorrelates with distance s along streamlines and is described by a spatial Markov process with respect to spatial correlation length ℓ . These studies were applied to (multi-log Gaussian) hydraulic conductivity fields with a well-defined minimum correlation length scale, similar to those considered in § 5. It has also been shown (Lester *et al.* 2022) that the velocity gradient in steady Darcy flow is also spatially Markovian, hence fluid deformation is characterised by sampling the dimensionless velocity gradient tensor $\epsilon'(t; X) \equiv \nabla \mathbf{v}(\mathbf{x}(t; X))^T \ell / \langle v_1 \rangle$ equidistantly with distance s along streamlines. Rotation into the Protean coordinate frame \mathbf{x}' (Lester *et al.* 2018a) renders the velocity gradient tensor $\epsilon'(t; X)$ upper triangular (see Appendix B for details) and the fluid deformation gradient tensor $\mathbf{F}'(t; X)$ which evolves as

$$\frac{d\mathbf{F}'(t; X)}{dt} = \epsilon'(t; X) \cdot \mathbf{F}'(t; X), \quad \mathbf{F}'(0; X) = \mathbf{1}, \quad (3.15)$$

is likewise. The diagonal elements F'_{ii} represent principal stretches and the off-diagonal components F'_{ij} (non-zero for $j > i$) represent shear deformations. Hence, the hyperbolic stretches that govern the Lyapunov exponents are given by the diagonal components ϵ'_{ii} , and are not conflated with shear deformations given by the off-diagonal components ϵ'_{ii} . From (3.15), the diagonal elements of $\mathbf{F}'(t; X)$ grow exponentially as

$$F'_{ii}(t; X) = \exp \left[\int_0^t dt' \epsilon'_{ii}(t'; X) \right], \quad i = 1, 2, 3. \quad (3.16)$$

For $i = 1$, this yields

$$F'_{11}(t; X) = \exp \left[\int_0^t dt' \frac{\partial v}{\partial s} \right] = \exp \left[\int_{v(0; X)}^{v(t; X)} dv' \frac{1}{v} \right] = \frac{v(t; X)}{v(0; X)}, \quad (3.17)$$

where s is the distance along the streamline labelled by X and $v(t; X) = ds/dt$. From (3.17), fluid stretching in the streamwise direction simply fluctuates with the local velocity as $F'_{11}(t) = v(t)/v(0)$, hence $\langle \epsilon'_{11}(t) \rangle = 0$. As $\sum_i \epsilon'_{ii} = 0$ for divergence-free flow flows, the Lyapunov exponent is then

$$\lambda_\infty = \langle \epsilon'_{22} \rangle = -\langle \epsilon'_{33} \rangle, \quad (3.18)$$

where $\langle \cdot \rangle$ denotes spatial averaging along streamlines. Hence, $F'_{22} \sim \exp(\lambda_\infty t)$ and $F'_{33} \sim \exp(-\lambda_\infty t)$, and so chaotic advection in steady 3-D flow is characterised by the single Lyapunov exponent λ_∞ .

In Appendix C we show that (3.16) leads to an *ab initio* continuous time random walk (CTRW) for the relative stretch $\rho \equiv \delta l(X, t)/\delta l(X, 0)$ of infinitesimal fluid line elements along streamlines as

$$\begin{aligned} \ln \rho_{n+1} &= \ln \rho_n + \frac{\ell \epsilon_n}{v_n}, \\ t_{n+1} &= t_n + \tau_n = t_n + \frac{\ell}{v_n}, \\ s_{n+1} &= s_n + \ell, \end{aligned} \quad (3.19)$$

where v_n and τ_n respectively are the streamline velocity magnitude and advection time between s_n and s_{n+1} and ϵ_n is the relevant Protean velocity gradient component ϵ'_{22} . The distribution $\psi(\tau)$ of waiting times τ is related to the Lagrangian velocity distribution $p_s(v)$ as

$$\psi(\tau) = \frac{\ell p_s(\ell/\tau)}{\tau^2}, \quad (3.20)$$

and $p_s(v) = v p_e(v)/\langle v \rangle_e$ (Dentz *et al.* 2016), where $p_e(v)$ is the Eulerian velocity distribution and $\langle \cdot \rangle_e$ represents an Eulerian average. For heterogeneous Darcy flow the Lagrangian velocity distribution may be heavy-tailed in the small velocity limit (Berkowitz *et al.* 2006), i.e. $p_s(v) \propto v^{\beta-1}$, $\beta > 1$ for $v \ll \langle v \rangle$ depending on the distribution of hydraulic conductivity (Hakoun, Comolli & Dentz 2019). Thus, the waiting time distribution scales as (Dentz *et al.* 2016)

$$\psi(\tau) \approx \frac{\psi_0}{|\Gamma(-\beta)|} t^{-1-\beta} \quad \text{for } \tau/\langle \tau \rangle \gg 1, \quad (3.21)$$

where Γ is the Gamma function and the q th-order moments $\langle \tau^q \rangle$ of $\psi(\tau)$ are finite for $q < \lfloor \beta \rfloor$. Hence, normal transport arises if $\beta > 2$, as the mean and variance of $\psi(\tau)$ are bounded, but anomalous transport arises for $1 < \beta < 2$ as the variance of $\psi(\tau)$ is unbounded. For $\beta > 1$, the advection time t_n may be related to the number of increments n as

$$t_n = \sum_{i=1}^n \tau_i \approx n \langle \tau \rangle = n \ell \left\langle \frac{1}{v_n} \right\rangle = \frac{n \ell}{\langle v \rangle_e} = n \tau_c, \quad (3.22)$$

where $\tau_c \equiv \ell/\langle v \rangle_e$ is the mean transition time. Similarly, the mean of $\ln \rho$ also grows linearly in time as $\langle \ln \rho \rangle = \langle \epsilon_n \rangle t = \lambda_\infty t$. The rate of growth of the variance $\sigma_{\ln \rho}^2$ serves as an important input parameter for lamellar mixing theories (Le Borgne, Dentz & Villiermaux 2015; Villiermaux 2019) that predict evolution of the concentration probability distribution function (PDF) for advective–diffusive solute transport from fluid stretching behaviour. Rebenshtok *et al.* (2014) and Dentz *et al.* (2015) show that in the asymptotic limit the coupled CTRW (3.19) generates q th-order absolute central moments μ_q for $q > \beta$ which scale as

$$\mu_q(t) \equiv \lim_{t \rightarrow \infty} \langle |\ln \rho - \lambda_\infty t|^q \rangle \sim \begin{cases} t^{1+q-\beta} & \text{for } 1 < \beta < 2, \\ t^{q/2} & \text{for } \beta > 2, \end{cases} \quad (3.23)$$

hence anomalous transport ($\beta < 2$) in heterogeneous 3-D Darcy flow can also generate anomalous stretching dynamics. In Appendix C we show for the case $\beta > 2$, $p_{\ln \rho}(\ln \rho)$ converges to a normal distribution with mean and variance

$$\lim_{t \rightarrow \infty} \langle \ln \rho \rangle = \lambda_\infty t \quad \lim_{t \rightarrow \infty} \sigma_{\ln \rho}^2 = \sigma_\lambda^2 t, \quad (3.24)$$

where $\sigma_\lambda^2 \equiv \sigma_\epsilon^2 \langle \tau^2 \rangle / \tau_c$ and σ_ϵ^2 is the variance of $p_\epsilon(\epsilon)$. For the anomalous stretching case ($1 < \beta < 2$), the variance $\sigma_{\ln \rho}^2$ growth ranges from normal to ballistic as (Dentz *et al.* 2015)

$$\lim_{t \rightarrow \infty} \sigma_{\ln \rho}^2 = \frac{\psi_0 \beta \Gamma(\beta + 1)}{6 - 5\beta + \beta^2} t^{3-\beta}. \quad (3.25)$$

Under such anomalous stretching the equality (3.2) between h and λ_∞ persists as temporal averaging along streamlines still dominates (Lester & Dentz 2025), but convergence of (3.1) slows as $\beta \downarrow 1$ and physical processes such as mixing and dispersion may be

impacted in this limit. In §5, we find that the flows considered herein all exhibit normal transport. However, anomalous stretching dynamics form an important kinematic regime that warrants future investigation.

4. Mechanisms of chaotic advection

In this section we consider the mechanisms that generate chaotic advection in steady 3-D Darcy flows ranging from periodic to random Darcy flows, and flows with smooth, finite $\mathbf{K}(\mathbf{x})$ to those with impermeable inclusions, non-smooth conductivity fields or stagnation points.

4.1. Chaotic advection in periodic Darcy flow

We first examine steady 3-D Darcy flows with a smooth, finite, heterogeneous and anisotropic hydraulic conductivity field $\mathbf{K}(\mathbf{x})$ that is P -periodic in the direction of the mean potential gradient $\mathbf{g} \equiv -\langle \nabla \phi \rangle / ||\langle \nabla \phi \rangle||$, i.e.

$$\mathbf{K}(\mathbf{x}) = \mathbf{K}(\mathbf{x} + nP\mathbf{g}), \quad n = 1, 2, \dots \quad (4.1)$$

The transform (3.6) ensures this flow has the same dynamics as a divergence-free temporally periodic flow (Bajer 1994; Speetjens *et al.* 2021), in that the advection equations can be cast as a time-periodic Hamiltonian system (often referred to as a 1(1/2) degree of freedom Hamiltonian system). As such, the established tools and techniques of Hamiltonian chaos (Ottino 1989; Katok & Hasselblatt 1995) can be used to understand the mechanisms leading to chaotic mixing in these flows, including construction of a stroboscopic map known as a Poincaré section of the flow, which is generated by recording the position of streamlines in the flow in the plane normal to \mathbf{g} at integer multiples of P . From the Brouwer fixed point theorem (Brouwer 1911), there must exist period- k points \mathbf{x}_k (with $k = 1, 2, \dots$) in the Poincaré section, such that streamlines at \mathbf{x}_k are advected downstream to $\mathbf{x}_p + kP\mathbf{g}$. These dynamics and features are exactly the same as those that arise in steady 3-D duct flows (Bajer 1994; Speetjens *et al.* 2021).

Each periodic point \mathbf{x}_k belongs to a corresponding periodic orbit (streamline). As per Hamiltonian dynamical systems theory (Katok & Hasselblatt 1995), a periodic point may be classified as either a hyperbolic saddle point \mathbf{x}_H if the local fluid deformation over the k -period involves fluid stretching and contraction that is exponential in time, or an elliptic point \mathbf{x}_E if the local fluid deformation involves rotation only. The number of hyperbolic (n_H) and elliptic (n_E) points is governed by the Poincaré–Hopf theorem, which may be expressed as

$$n_E - n_H = 2(1 - g), \quad (4.2)$$

where g is the topological genus of the Poincaré section (which may be 0, 1 or 2 depending upon its periodicity). Elliptic points are associated with non-chaotic (non-mixing) regions of the flow known as Kolmogorov–Arnold–Moser (KAM) islands, where the local Lyapunov exponent is zero. For hyperbolic points, the directions of the exponentially stretching and contracting are respectively associated with hyperbolic unstable and stable manifolds emanating from \mathbf{x}_k . If these manifolds intersect transversely (which arises in all but highly symmetric systems (Haller & Poje 1998)), then a heteroclinic tangle results, leading to chaotic advection (Ottino 1989; Katok & Hasselblatt 1995) in these regions, with positive Lyapunov exponent.

The transition from globally non-chaotic to globally chaotic dynamics in Hamiltonian systems is well established, with three predominant ‘routes to chaos’ identified (period doubling, quasi-periodicity and intermittency) as system parameters are altered. In the

case of steady 3-D Darcy flows, these parameters are the degree of heterogeneity ($\sigma_{\ln K}^2$) or anisotropy (δ in § 5) of the conductivity field \mathbf{K} as either homogeneous or isotropic fields do not generate chaos. Under the period-doubling route, the increase of such control parameters leads to bifurcation of elliptic points into two elliptic and one hyperbolic point (thus maintaining (4.2)), and the stable and unstable manifolds associated with this hyperbolic point connect smoothly. However, with a further increase of the control parameters, these manifolds then intersect transversely, leading to a heteroclinic tangle, the hallmark of chaotic dynamics in Hamiltonian systems. This transition is associated with the formation of a chaotic ‘sea’ surrounding the two KAM ‘islands’ associated with the elliptic points. This process continues, with further bifurcation of elliptic points and growing chaotic regions associated with hyperbolic points until the domain is essentially filled with a chaotic sea and the KAM islands surrounding elliptic points are vanishingly small. In § 5 we demonstrate this route to chaos with increasing conductivity heterogeneity, including identification of periodic points and associated structures (KAM islands, hyperbolic manifolds).

4.2. Chaotic advection in random Darcy flow

For random Darcy flow, this picture is altered somewhat as there do not exist persistent features such as hyperbolic and elliptic periodic points, KAM islands and hyperbolic manifolds to elucidate the mixing dynamics of the flow. Instead, finite-time analogues of these features – elliptic, hyperbolic and parabolic LCS (Haller 2015) – serve to organise fluid motion and uncover the Lagrangian dynamics of the flow over finite time scales. One major difference for random flows is that all particle trajectories are now ergodic (Liu, Muzzio & Peskin 1994; Poje, Haller & Mezić 1999; Kang *et al.* 2008), meaning that statistics gathered over long times are equivalent to ensemble statistics as trajectories sample the entire phase space of the flow. This means that e.g. KAM islands cannot persist and all trajectories are chaotic, rather than a topologically distinct (in the Lagrangian frame) set of mixing and non-mixing regions. Hence, while elliptic and hyperbolic regions of the flow can be identified over finite periods, in the infinite time limit random flows are globally chaotic, and the finite-time Lyapunov exponent (FTLE) of each 3-D streamline converges to the unique global Lyapunov exponent of the flow (due to ergodicity). As the flow control parameter is increased from zero to finite values, the flow transitions from integrable (regular) dynamics to fully chaotic, and the Lyapunov exponent steadily increases from zero to finite values. A similar picture emerges if the flow is analysed via the braiding analogue of the FTLE, finite-time braiding exponent (FTBE) (Budišić & Thiffeault 2015). Similar to the FTLE, for periodic flows the FTBE is zero inside KAM islands as the streamlines only undergo trivial braiding, and the FTBE is positive in chaotic regions due to non-trivial braiding with positive topological entropy. Conversely, for random chaotic Darcy flows the FTBE is positive everywhere at long times as all streamlines undergo non-trivial braiding due to ergodicity. As such, we make the conjecture that, similar to other aperiodic Hamiltonian systems (Liu *et al.* 1994; Poje *et al.* 1999), if an aperiodic Darcy flow exhibits chaotic trajectories, it must be globally chaotic due to ergodicity of streamlines. This conjecture has important implications for interpreting the results in § 5.

4.3. Chaotic advection from non-finite or non-smooth hydraulic conductivity

Although beyond the scope of this study, it is useful to briefly discuss the generation of chaos in steady Darcy flows with stagnation points or non-smooth hydraulic conductivity. For steady 3-D Darcy flow with non-finite conductivity fields (associated

with impermeable inclusions) or boundary conditions or flow sources and sinks that generate stagnation points, chaotic advection can also arise in the absence of anisotropy of the hydraulic conductivity field. For these flows, as $v_\phi \downarrow 0$ at stagnation points \mathbf{x}_p , the rescaling (3.7) breaks down (Bajer 1994), leading to chaotic advection via a similar mechanism to that of pore-scale flow (Lester *et al.* 2013). Here, exponential stretching of fluid elements local to saddle-type stagnation points (Surana, Grunberg & Haller 2006) (an analogue of hyperbolic periodic points) form stable and unstable hyperbolic manifolds in the flow. Under symmetry breaking, these hyperbolic manifolds form a heteroclinic tangle, the hallmark of chaos in continuous dynamical systems (Ottino 1989; Katok & Hasselblatt 1995). For steady Darcy flows with isotropic but non-smooth heterogeneous conductivity fields \mathbf{K} , the velocity gradient, vorticity and helicity are undefined over discontinuities in $\nabla \mathbf{K}$, leading to ‘leakage’ of streamlines from coherent streamsheets and the potential for chaos (Lester *et al.* 2023). This mechanism is not well understood and it is currently unclear whether such discontinuities in $\nabla \mathbf{K}$ are physically realistic, or a consequence of the breakdown of the Darcy approximation at small scales.

5. Chaotic advection in heterogeneous Darcy flow

5.1. Onset of chaotic advection with anisotropy

The results in § 3 uncover a deep link between chaotic advection and transverse dispersion in heterogeneous Darcy flow, and show how anomalous transport generates anomalous stretching dynamics. To examine the onset of chaotic advection with medium anisotropy, we first consider Darcy flow in the simplest possible conductivity field that admits non-zero helicity

$$\mathbf{K}(\mathbf{x}) = k_0(\mathbf{x})\mathbf{I} + \delta[k_\delta(\mathbf{x}) - k_0(\mathbf{x})]\hat{\mathbf{e}}_1 \otimes \hat{\mathbf{e}}_1, \quad (5.1)$$

where $k_0(\mathbf{x}) \neq k_\delta(\mathbf{x})$ and $\delta \in [0, 1]$ quantifies anisotropy of the conductivity tensor. Although this flow has been previously considered (Lester *et al.* 2024) in the context of quantifying the link between stirring and dispersion, here, we focus on the onset of chaotic dynamics with δ . Note that, while similar conductivity tensor fields such as $\mathbf{K}(\mathbf{x}) = k_0(\mathbf{x})(\mathbf{I} + \delta\hat{\mathbf{e}}_1 \otimes \hat{\mathbf{e}}_1)$ have non-zero helicity density $\mathcal{H}(\mathbf{x}) \neq 0$, the resulting flows are shown (Appendix A) to be epi-two-dimensional (Yoshida & Morrison 2017) and hence non-chaotic (Arnol’d 1965; Holm & Kimura 1991).

Darcy flow over the conductivity field (5.1) is driven by a unit potential gradient $\nabla\bar{\phi} = \{-1, 0, 0\}$ in a triply periodic unit cube (3-torus \mathbb{T}^3) $\Omega : \mathbf{x} \in [0, 1] \times [0, 1] \times [0, 1]$, and the scalar log-conductivity fields $f(\mathbf{x}) \equiv \ln k(\mathbf{x})$ for the independent fields $k_0(\mathbf{x})$, $k_\delta(\mathbf{x})$ are given by

$$f(\mathbf{x}) = \Sigma_{\ln K}^2 \sum_{n=1}^{N_i} \sum_{i,j,k}^N \frac{A_{n,ijk}}{\sqrt{i^2 + j^2 + k^2}} \cos[2\pi i(x_1 + \chi_{n,ijk}^1)] \cos[2\pi j(x_2 + \chi_{n,ijk}^2)] \cos(2\pi k(x_3 + \chi_{n,ijk}^3)), \quad (5.2)$$

with $N = 4$ and so the velocity correlation length scale is $\ell = 1/(2N)$. Here, $N_i = 2$ is the number of realisations in each mode, and $A_{n,ijk}$ and $\chi_{n,ijk}^m$ with $m = 1, 2, 3$ are uniformly distributed random variables in $[0, 1]$. The coefficient $\Sigma_{\ln K}$ is chosen such that the log variance of the conductivity field is $\|f^2\|_\Omega = \sigma_{\ln K}^2 = 4$. A typical scalar field $f(\mathbf{x})$ with these parameters is shown in figure 1(a). Note fields with $N = 1$ do not generate a chaotic dynamics due to symmetry of the velocity field.

To solve the divergence-free condition $\nabla \cdot \mathbf{v} = 0$ over Ω , ϕ is decomposed into a mean and fluctuation as

$$\phi(\mathbf{x}) = \bar{\phi}(\mathbf{x}) + \tilde{\phi}(\mathbf{x}), \quad (5.3)$$

where $\bar{\phi} = -x_1$. From (2.2), $\tilde{\phi}(\mathbf{x})$ is governed by

$$\nabla \cdot (\mathbf{K} \cdot \nabla \tilde{\phi}(\mathbf{x})) - \nabla \cdot (\mathbf{K} \cdot \hat{\mathbf{e}}_1) = 0. \quad (5.4)$$

Methods to solve (5.4) and perform streamline tracking are detailed in Appendix D, and typical potential fields and streamlines are shown in figure 1. For each value of δ , a realisation of $\mathbf{K}(\mathbf{x})$ is generated, (5.4) is solved and 10^3 3-D streamlines are computed for distance $10^4 \ell$, along with the transverse dispersion coefficient D_T , Protean velocity gradient tensor ϵ' and Lyapunov exponent $\lambda_\infty = \langle \epsilon'_{22} \rangle$, as described in Appendix C.

Typical streamfunctions $\psi_1(\mathbf{x})$, $\psi_2(\mathbf{x})$ for the helicity-free flow $\delta = 0$ given by (2.7) (see Appendix D for solution details) are shown in figure 6(a). Streamlines (green) are confined to the intersections of the level sets of ψ_1 and ψ_2 , and their global behaviour is shown in figure 1(c). Despite their significant tortuosity, these confined streamlines do not exhibit persistent dispersion or non-trivial braiding. Conversely, for $\delta > 0$ the associated streamlines (red) in figure 6(a) are unconfined and so exhibit streamline braiding and transverse dispersion, see also figure 1(d) for $\delta = 1$.

Figure 6(b) shows that the mean helicity magnitude $\langle |\mathcal{H}| \rangle$ increases from $\mathcal{H}(\mathbf{x}) = 0$ everywhere for $\delta = 0$ to a plateau $\langle |\mathcal{H}| \rangle \approx 4.74$ at $\delta = 0.9$, then suddenly increases to $\langle |\mathcal{H}| \rangle \approx 7.16$ at $\delta = 1$. This sharp increase as $\delta \uparrow 1$ is attributed to the loss of correlation between the K_{11} and $K_{22} = K_{33}$ fields. The linear growth of $\langle |\mathcal{H}| \rangle$ for $\delta \ll 1$ is explained by decomposing the potential field ϕ as $\phi(\mathbf{x}) = \phi_0(\mathbf{x}) + \delta \phi_\delta(\mathbf{x})$. To leading order $\mathbf{v}(\mathbf{x})$ is then

$$\mathbf{v}(\mathbf{x}) = \mathbf{v}_0(\mathbf{x}) + \delta \mathbf{v}_\delta(\mathbf{x}), = -k_0 \nabla \phi_0 - \delta [k_0 \nabla \phi_\delta - k_\delta \hat{\mathbf{e}}_1 (\hat{\mathbf{e}}_1 \cdot \nabla \phi_0)] + \mathcal{O}(\delta^2), \quad (5.5)$$

where $\mathbf{v}_0(\mathbf{x})$ is helicity free and the helical perturbation $\mathbf{v}_\delta(\mathbf{x})$ is generated by the difference $k_0 - k_\delta$, as is shown by inserting (5.5) into $\mathcal{H}(\mathbf{x}) \equiv \mathbf{v} \cdot (\nabla \times \mathbf{v})$ and truncating to order δ to give

$$\begin{aligned} \mathcal{H}(\mathbf{x}) = & \delta [k_0 \nabla \phi \cdot (\hat{\mathbf{e}}_1 \times \nabla (k_\delta - k_0) (\nabla \phi \cdot \hat{\mathbf{e}}_1)) \\ & + (k_\delta - k_0) (\nabla \phi \cdot \hat{\mathbf{e}}_1 \otimes \hat{\mathbf{e}}_1 \cdot (\nabla k_0 \times \nabla \phi))] + \mathcal{O}(\delta^2). \end{aligned} \quad (5.6)$$

Figure 6(c) shows D_T increases exponentially with δ as

$$\frac{D_T}{\langle v_1 \rangle \ell} = \frac{1}{Pe_T} \approx 4.343 \times 10^{-6} (e^{10.214 \delta} - 1), \quad (5.7)$$

which is consistent with (2.7) as $D_T = 0$ for $\delta = 0$ (Lester *et al.* 2023), indicating finite transverse dispersion arises for weak perturbations away from heterogeneous isotropic Darcy flow. Figure 6(d) shows that λ_∞ also increases exponentially with δ as

$$\lambda_\infty \approx 0.00381 (e^{5.283 \delta} - 1), \quad (5.8)$$

and is also non-zero for small $\delta > 0$, indicating that chaotic advection occurs for weak perturbations away from isotropic Darcy flow. For $\delta = 0$ the streamfunction formulation (2.7) enforces zero Lyapunov exponent (Lester *et al.* 2022). Figure 6(d) also shows that insertion of the fitted exponential (5.8) for D_T into a similar relationship to (3.14)

$$\lambda_\infty = 2 \sqrt{\frac{D_T}{\langle v_1 \rangle \ell}}, \quad (5.9)$$

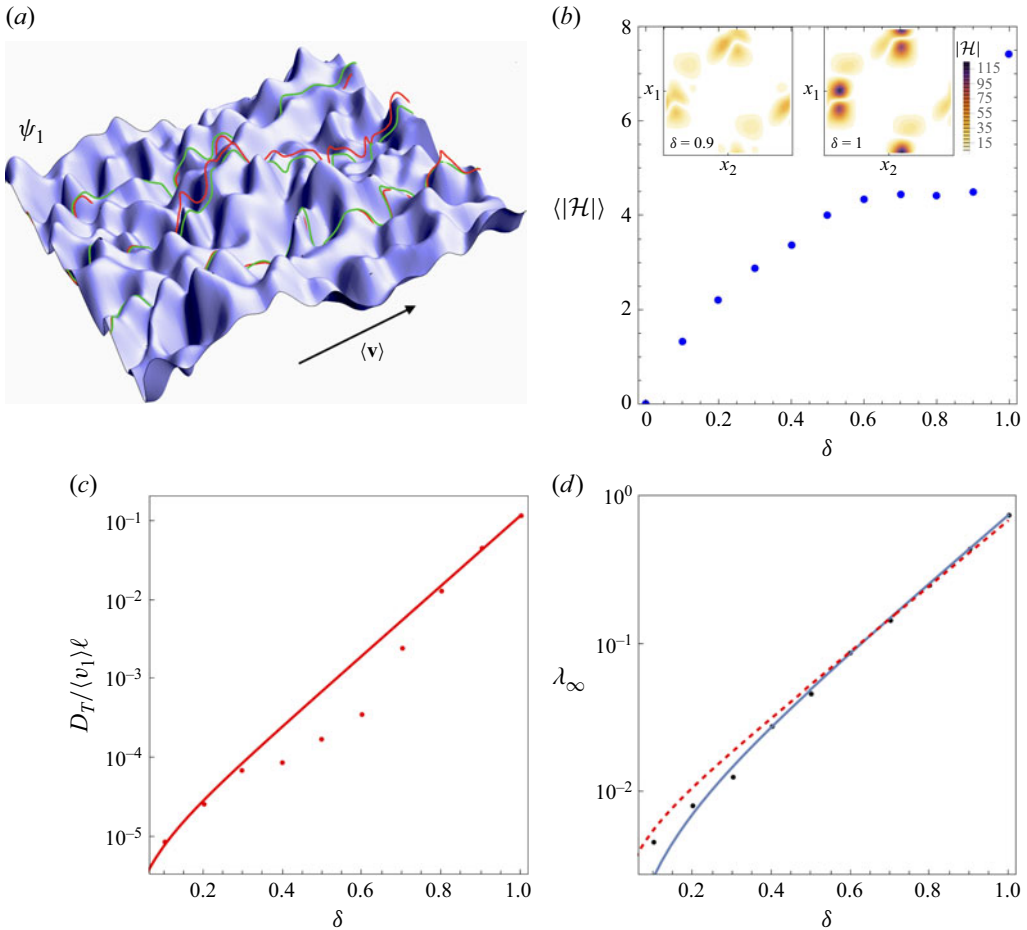


Figure 6. (a) Perturbation of $\delta = 0.1$ streamlines (red) from $\delta = 0$ (zero helicity) streamlines (green) and associated ψ_1 streamsurface (blue) for the conductivity field given in (5.1). Similar perturbation of $\delta = 0.1$ streamlines away from the ψ_2 streamsurfaces (not shown) also occurs. (b) Growth of mean absolute helicity $\langle |\mathcal{H}| \rangle$ with δ , inset shows $|\mathcal{H}|$ fields for $\delta = 0.9, 1$ (adapted from Lester *et al.* 2024). (c) Growth of transverse dispersion coefficient $D_T / \langle v_1 \rangle \ell$ with δ from simulations (red points) and fitted exponential (5.7) (red curve). (d) Growth of Lyapunov exponent λ_∞ with perturbation parameter δ from simulations (black points) and fitted exponential (5.8) (blue curve). Also shown (red dotted curve) is the dimensionless Lyapunov exponent λ_∞ predicted from fitted exponential in (b) and (3.14). (c), (d) Adapted from (Lester *et al.* 2024).

yields excellent agreement with the measured Lyapunov exponent in (5.7). The different proportionality between λ_∞ and D_T to (3.14) is expected as the domain Ω is finite and so does not belong to a universality class (Ódor 2004). These results indicate that chaotic advection is inherent to anisotropic heterogeneous Darcy flow. If the conjecture raised in § 4.2 is true, this statement also holds for weakly anisotropic random heterogeneous conductivity fields.

5.2. Onset of chaotic advection with medium heterogeneity

To examine the impact of medium heterogeneity upon anisotropic Darcy flow, we consider flow generated by the anisotropic diagonal conductivity tensor $\mathbf{K}(\mathbf{x})$ in (2.4), where the scalar conductivity fields K_{ii} are generated in the same manner as k_0, k_δ but with

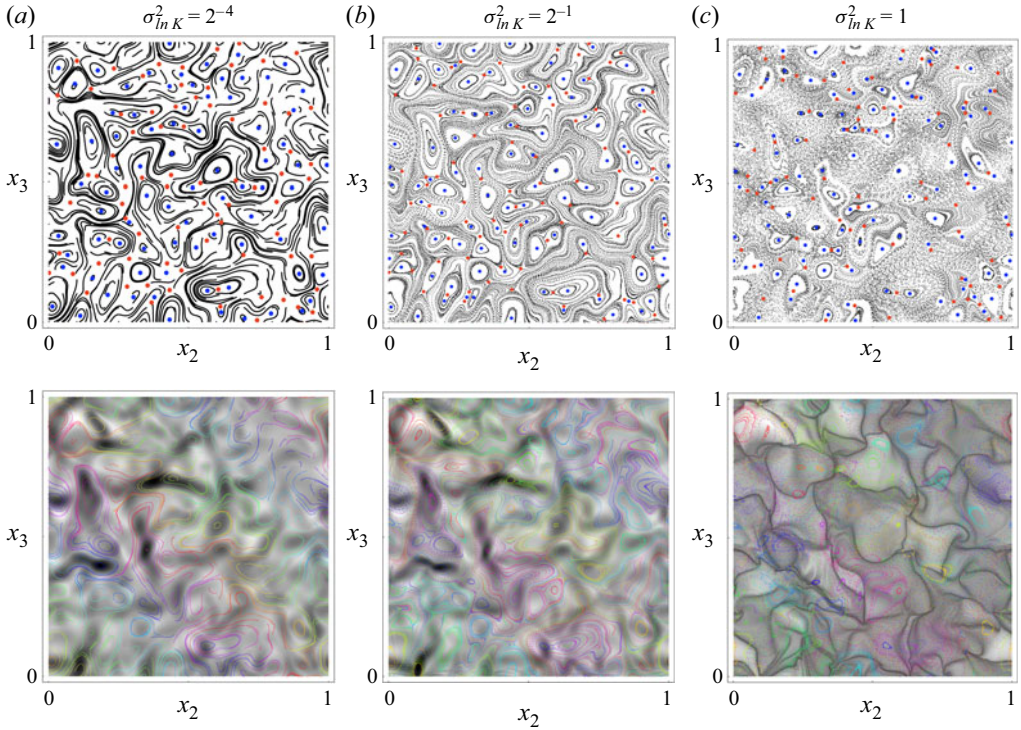


Figure 7. (Top row) Poincaré sections and (bottom row) FTLE fields with superposed Poincaré sections (colours used to distinguish different streamlines) of steady 3-D anisotropic Darcy flow ranging from weakly ($\sigma_{\ln K}^2 = 2^{-4}$) to moderately ($\sigma_{\ln K}^2 = 1$) heterogeneous conductivity fields. Blue and red points respectively denote elliptic (x_E) and hyperbolic (x_H) points. Note for more heterogeneous conductivity fields $\sigma_{\ln K}^2 \geq 2$ (not shown), the KAM islands shrink to infinitesimal size, indicating essentially globally chaotic dynamics.

$N_i = 4$. The heterogeneity of these fields K_{ii} is varied from weakly ($\sigma_{\ln K}^2 < 1$) to strongly ($\sigma_{\ln K}^2 > 1$) heterogeneous over the range of log variances $\sigma_{\ln K}^2 = (2^{-10}, 2^{-8}, \dots, 2^{-2}) \cup (1/2, 1, 2, 3, 4)$. For each value of $\sigma_{\ln K}^2$, a realisation of $\mathbf{K}(\mathbf{x})$ is generated and (5.4) is solved, and streamlines, D_T and λ_∞ are computed in the same manner as described in § 5.1.

Figure 7 shows both contour plots of the FTLE $\lambda(t, \mathbf{X})$ and Poincaré sections and low-order ($k = 1, 2, 3$) periodic points for the cases $\sigma_{\ln K}^2 = 2^{-4}, 2^{-1}, 1$, where the log variance $\sigma_{\ln K}^2$ acts as a control parameter that governs perturbation from the non-chaotic (integrable) state corresponding to homogeneous anisotropic Darcy flow with $\sigma_{\ln K}^2 = 0$. The FTLE field is computed using the LCS Tool package (Onu, Huhn & Haller 2015 for the analogous 2-D unsteady flow via the transform (3.6)), where the FTLE field is computed over one period of the flow $t \in [0, 1]$ as

$$\lambda(t; \mathbf{X}) = \frac{1}{2t} \ln \sigma_{\max}(t; \mathbf{X}), \quad (5.10)$$

for $\mathbf{X} \in x_2 \times x_3 = [0, 1] \times [0, 1]$ where $\sigma_{\max}(t; \mathbf{X})$ is the largest eigenvalue of the Cauchy–Green tensor $\mathbf{C}(t; \mathbf{X}) \equiv \mathbf{F}(t; \mathbf{X})^\top \cdot \mathbf{F}(t; \mathbf{X})$. The Poincaré sections indicate that even for very weak heterogeneity ($\sigma_{\ln K}^2 = 2^{-4}$), the Lagrangian topology is rich, consisting of a large number of elliptic and hyperbolic points, with a greater number density than that suggested by the correlation length ℓ . For such weak heterogeneity, the

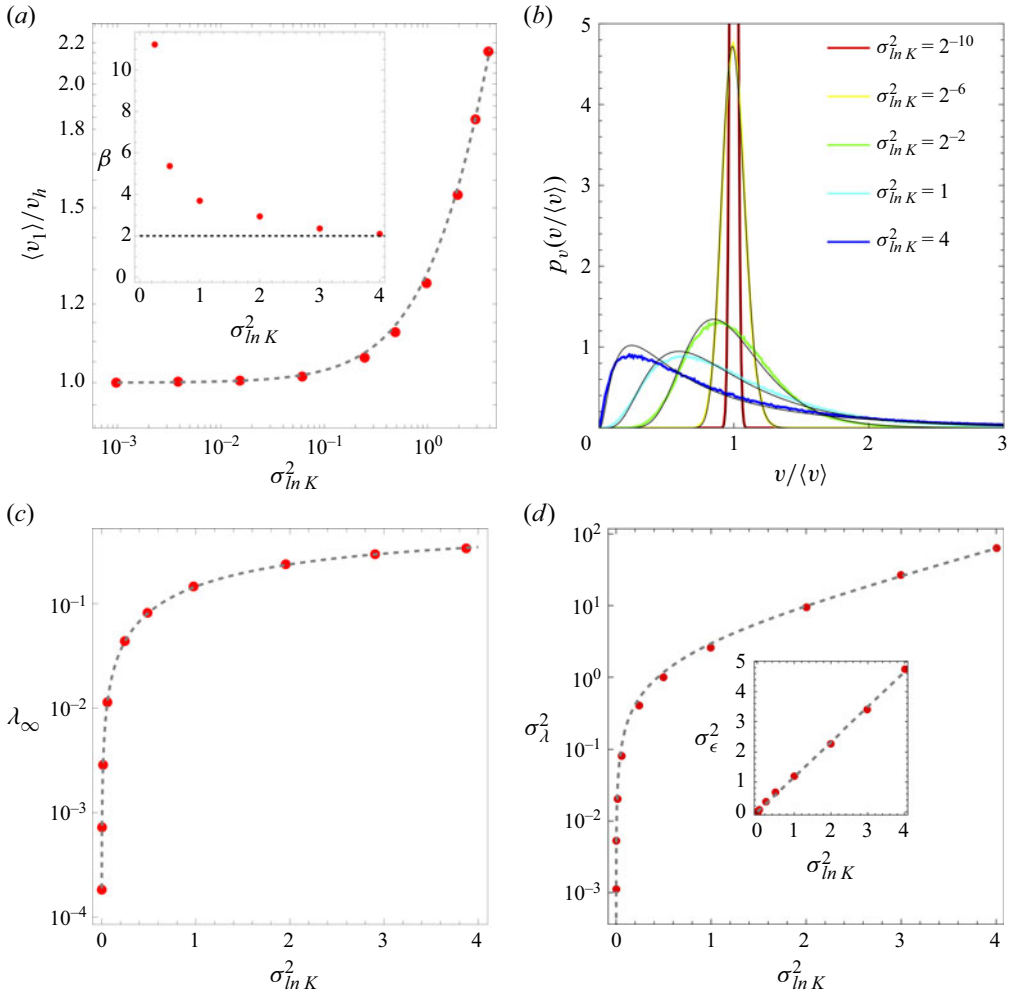


Figure 8. (a) Variation of normalised mean longitudinal velocity $\langle v_1 \rangle / v_h$ (red points) with log variance $\sigma_{\ln K}^2$ and linear fit (5.14), (grey dashed line) in anisotropic Darcy flow. (Inset) Variation of small velocity scaling index β with $\sigma_{\ln K}^2$. (b) The PDFs of normalised velocity magnitude $p_v(v/\langle v \rangle)$ as a function of log variance $\sigma_{\ln K}^2$ and fitted log-normal distribution (black lines). (c) Variation of dimensionless Lyapunov exponent λ_∞ (red dots) with log variance $\sigma_{\ln K}^2$ and nonlinear fit (5.19), (grey dashed line). (d) Variation of dimensionless stretching variance σ_λ^2 with log variance $\sigma_{\ln K}^2$ and nonlinear fit (5.16), (grey dashed line). (Inset) Variation of Protean velocity gradient variance σ_ϵ^2 with log variance $\sigma_{\ln K}^2$ and linear fit (5.15), (grey dashed line).

Lagrangian dynamics are close to integrable, with stable and unstable manifolds (not shown) associated with hyperbolic points intersecting almost tangentially, corresponding to weakly chaotic dynamics, as reflected by the small Lyapunov exponent reported in figure 8(c). The integrable nature of this weakly heterogeneous flow is also established by considering the non-zero diagonal components $K_{ii}(\mathbf{x})$ of $\mathbf{K}(\mathbf{x})$ in the limit $\sigma_{\ln K}^2 \rightarrow 0$, such that $K_{ii}(\mathbf{x}) = \exp(\sigma_{\ln K} f_{ii}(\mathbf{x})) \approx 1 + \sigma_{\ln K} f_{ii}(\mathbf{x})$, hence

$$\mathbf{K}(\mathbf{x}) \approx \mathbf{I} + \sigma_{\ln K} \mathbf{f}(\mathbf{x}), \quad \phi(\mathbf{x}) \approx x_1 + \sigma_{\ln K} \tilde{\phi}(\mathbf{x}), \quad (5.11)$$

where $\mathbf{f}(\mathbf{x}) \equiv \sum_{i=1}^3 f_{ii}(\mathbf{x}) \hat{\mathbf{e}}_i \otimes \hat{\mathbf{e}}_i$, and the potential fluctuation $\tilde{\phi}$ and velocity field satisfy

$$\nabla^2 \tilde{\phi} + \nabla f_{11}(\mathbf{x}) \cdot \hat{\mathbf{e}}_1 = 0, \quad \mathbf{v}(\mathbf{x}) = -\hat{\mathbf{e}}_1 - \sigma_{lnK} [f_{11}(\mathbf{x}) \hat{\mathbf{e}}_1 + \nabla \tilde{\phi}] + \mathcal{O}(\sigma_{lnK}^2). \quad (5.12)$$

Hence, to leading order, the perturbative flow is solely driven by $f_{11}(\mathbf{x})$ and the helicity density scales with σ_{lnK}^2 as

$$\mathcal{H}(\mathbf{x}) = \sigma_{lnK}^2 \hat{\mathbf{e}}_1 (\nabla \tilde{\phi} \times \nabla f_{11}) + \mathcal{O}(\sigma_{lnK}^3), \quad (5.13)$$

so this flow is integrable in the limit $\sigma_{lnK}^2 \rightarrow 0$, and the perturbation that scales with σ_{lnK}^2 in (5.12) is heterogeneous and anisotropic. Hence, this perturbation represents a non-integrable perturbation away from a fully integrable state, and so shares the same basic features as non-integrable perturbation of integrable Hamiltonian systems. With increasing medium heterogeneity, ($\sigma_{lnK}^2 = 2^{-1}$), the chaotic dynamics strengthen, with clearly visible stochastic layers (chaotic regions) between distinct KAM islands apparent in figure 7(b), but no bifurcation of low-order periodic points are apparent. As σ_{lnK}^2 grows to 1, evidence of period-doubling bifurcations in low-order periodic points become apparent as KAM islands break up into smaller islands. Other surviving integrable regions shrink further, before transitioning to essentially globally chaotic dynamics at $\sigma_{lnK}^2 = 2$ (not shown). These dynamics are also reflected by the FTLE distributions, which show some weakly negative regions that correspond to KAM islands as the analogous 2-D flow (3.6) is not divergence free but it is Hamiltonian (Bajer 1994). For weak ($\sigma_{lnK}^2 = 2^{-4}$) to moderate ($\sigma_{lnK}^2 = 2^{-1}$) medium heterogeneity, the basic structure of the FTLE field is invariant up to a scaling factor, reflecting influence of the hydraulic conductivity field upon the fluid stretching dynamics. This behaviour, including the transition from an integrable state to global chaos under a non-integrable perturbation (in this case an anisotropic and heterogeneous perturbation) is entirely consistent with the embedded Hamiltonian structure of steady 3-D Darcy flow (Speetjens *et al.* 2021) discussed in § 3.2.

Figure 8(a) shows that the scaled mean longitudinal velocity $\langle v_1 \rangle / v_h$ (where v_h is the velocity for a homogeneous medium with the same mean permeability) increases linearly with log variance σ_{lnK}^2 as expected for small and moderate values of σ_{lnK}^2 (Renard & De Marsily 1997)

$$\frac{\langle v_1 \rangle}{v_h} = 1 + \alpha_1 \sigma_{lnK}^2, \quad (5.14)$$

with $\alpha_1 \approx 0.29178$ and coefficient of determination $R^2 = 0.999$. Figure 8(b) shows that the Eulerian velocity PDF $p_v(v)$ roughly follows a log-normal distribution for all but strongly heterogeneous flows, and converges toward a delta function in the homogeneous limit $\sigma_{lnK}^2 \rightarrow 0$. For $\sigma_{lnK}^2 \geq 1$, the velocity PDF scales as a power law in the small velocity limit as $p_v(v) \propto v^{\beta-1}$, and the inset in figure 8(a) shows that the index $\beta > 2$ and approaches $\beta \downarrow 2$ in the strongly heterogeneous regime, leading to normal transport for all $\sigma_{lnK}^2 \geq 1$. The persistence of normal transport in the strongly heterogeneous regime is attributed to the low probability of all three K_{ii} in (2.4) being simultaneously small. We also note that different random models such as Gamma-distributed conductivity fields have a greater propensity to generate anomalous transport (Hakoun *et al.* 2019).

Figure 8(c) shows that λ_∞ may converge to a constant value with increasing log variance σ_{lnK}^2 , and is well fitted by the simple nonlinear function (5.19) as described below. Although the numerical methods used do not allow flows in more heterogeneous media to be computed, asymptotic convergence of λ_∞ with increasing σ_{lnK}^2 is argued on

physical grounds. We consider the limit $\sigma_{lnK}^2 \rightarrow \infty$ and partition \mathbf{K} over Ω into infinitely permeable Ω_∞ ($\text{tr } \mathbf{K}(\mathbf{x}) \rightarrow \infty$) and impermeable Ω_0 ($\text{tr } \mathbf{K}(\mathbf{x}) \rightarrow 0$) subdomains. As Ω is the 3-torus \mathbb{T}^3 with topological genus $g = 3$, the boundary $\partial\Omega_{\infty 0}$ between the subdomains is also topologically complex and thus admits saddle-type stagnation points \mathbf{x}_0 on $\partial\Omega_{\infty 0}$ as per the Poincaré–Hopf theorem. As discussed in §4.3, these saddle points generate chaotic advection via the same mechanism as for pore-scale Stokes flow (Lester *et al.* 2013). Due to the linearity of Darcy flow, the rescaled fluid velocity field $\mathbf{v}/\langle v_1 \rangle$ and associated saddle points and Lyapunov exponent are all invariant in the limit $\sigma_{lnK}^2 \rightarrow \infty$.

As shown in the inset of figure 8(d), the velocity gradient variance σ_ϵ^2 (from data presented in §5.3) grows linearly with conductivity log variance as

$$\sigma_\epsilon^2 \approx \alpha_2 \sigma_{lnK}^2, \quad (5.15)$$

where $\alpha_2 = 1.1656$ with $R^2 = 0.999$, and σ_λ^2 grows exponentially with σ_{lnK}^2 as

$$\sigma_\lambda^2 \approx \alpha_3 (e^{\alpha_4 \sigma_{lnK}^2} - 1), \quad (5.16)$$

where $\alpha_3 = 2.2429$ and $\alpha_4 = 0.8415$ with $R^2 = 0.999$. These results show that, although the Lyapunov exponent λ_∞ converges toward the upper bound $\ln 2$ with increasing medium heterogeneity, the corresponding variance σ_λ^2 increases due to growth of the second moment $\langle \tau^2 \rangle$. For the case of anomalous transport ($1 < \beta < 2$), this variance grows super-linearly as $\sigma_{ln\rho}^2 \sim t^{3-\beta}$ Lester *et al.* (2018a).

In addition to direct computation of λ_∞ , the topological braid entropy h_{braid} of the streamlines is computed directly via the E-tec routine (Roberts *et al.* 2019), which is limited to moderately heterogeneous ($0.1 \leq \sigma_{lnK}^2 \leq 2$) systems due to lack of convergence for $\sigma_{lnK}^2 < 0.1$ and flow reversal for $\sigma_{lnK}^2 > 1$. In principle, streamlines for the strongly heterogeneous cases could be placed in the intrinsic coordinates $\boldsymbol{\xi} = (\chi_1, \chi_2, \phi)$, however, determination of χ_1, χ_2 is difficult as the non-zero helicity density $\mathcal{H}(\mathbf{x}) \neq 0$ means that mutual Lie derivatives of the flow do not vanish and so there does not exist an intrinsic holonomic basis (Schutz 1980) (a coherent orthogonal coordinate system) for (χ_1, χ_2) . Figure 9(a) shows that λ_∞ and h_{braid} agree to within 5 %, verifying (3.2).

In the weakly heterogeneous regime ($\sigma_{lnK}^2 \leq 1$), λ_∞ varies almost linearly with log variance as

$$\lambda_\infty \approx \alpha_6 (\sigma_{lnK}^2)^{\alpha_5}, \quad (5.17)$$

with $\alpha_6 = 0.154$, $\alpha_5 = 1.129$ and $R^2 = 0.995$, suggesting that chaotic advection arises in weakly heterogeneous anisotropic conductivity fields. Figure 9(b) shows that in the strongly heterogeneous regime, λ_∞ scales linearly with σ_{lnK}^2 as

$$\lambda_\infty \frac{\langle v_1 \rangle}{v_h} \approx \alpha_7 \sigma_{lnK}^2, \quad (5.18)$$

with $\alpha_7 \approx 0.198$ and $R^2 = 0.999$. Dividing by (5.14) yields

$$\lambda_\infty \approx \frac{\alpha_7 \sigma_{lnK}^2}{1 + \alpha_1 \sigma_{lnK}^2}, \quad (5.19)$$

which, as shown in figure 8(c), provides an excellent fit of λ_∞ as a function of σ_{lnK}^2 across the entire regime. Note that (5.19) is compatible with (5.17) in the weakly heterogeneous limit $\sigma_{lnK}^2 \ll 1$ under the approximation $\alpha_5 \approx 1$ as $\alpha_6 \approx \alpha_7/(1 + \alpha_1) = 0.1538$. Equation

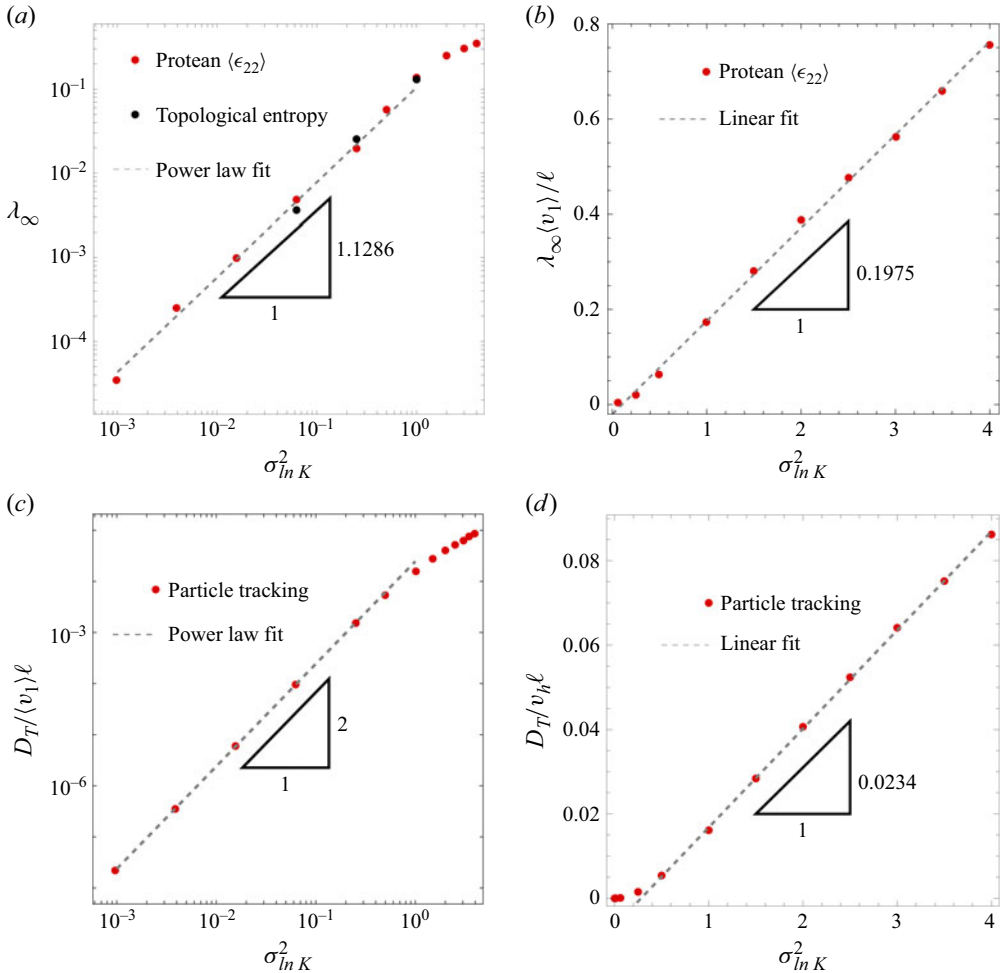


Figure 9. (a,b) Lyapunov exponents and (c,d) dispersion coefficients in (a,c) weakly ($\sigma_{\ln K}^2 \leq 1$) and (b,d) strongly ($\sigma_{\ln K}^2 \geq 1$) heterogeneous porous media with anisotropic conductivity given by (2.4). Red points in (a,b) indicate Lyapunov exponents computed from the Protean (Lester *et al.* 2018a), black points indicate topological entropy computed using E-tec (Roberts *et al.* 2019). Dashed lines in (a,c) and (b,d) respectively indicate power law (5.17), (5.21), and linear (5.18), (5.22), fits to the Lyapunov exponents and dispersion coefficients in the weakly and strongly heterogeneous regimes.

(5.19) also implies that λ_∞ converges in the strongly heterogeneous limit

$$\lim_{\sigma_{\ln K}^2 \rightarrow \infty} \lambda_\infty \approx \frac{\alpha_7}{\alpha_1} = 0.677. \quad (5.20)$$

This value is close to the upper bound $h = \ln 2 \approx 0.693$ for steady 3-D flow (Dinh & Sibony 2008), indicating strong chaotic mixing arises in strongly heterogeneous anisotropic Darcy flow.

Figure 9(c) shows that the transverse dispersion coefficient scales nonlinearly in the weakly heterogeneous regime as

$$\frac{D_T}{\langle v_1 \rangle l} \sim (\sigma_{\ln K}^2)^{2.01}, \quad (5.21)$$

and figure 9(d) shows that transverse dispersion coefficient scales linearly in the strongly heterogeneous regime as

$$\frac{D_T}{v_h \ell} \approx 0.0234 \sigma_{lnK}^2, \quad (5.22)$$

with $R^2 = 1.000$ in both cases. In the weakly heterogeneous regime, the scalings of D_T (5.21) and λ_∞ (5.17) with σ_{lnK}^2 agree with the relationship (3.14) linking dispersion and chaotic advection in random flows. However, as expected this relationship does not persist in the strongly heterogeneous regime due to the onset of flow reversal. Similar to the findings in § 5.1, these results indicate that chaotic advection is inherent to heterogeneous anisotropic Darcy flow. If the conjecture raised in § 4.2 is true, this statement also holds for weakly heterogeneous random anisotropic conductivity fields.

5.3. Velocity gradient statistics

In addition to the Lyapunov exponent, the Protean velocity gradient ϵ' provides important information regarding the deformation structure of heterogeneous Darcy flow. For all computed flows ϵ' is sampled along 10^3 streamlines at fixed spatial increment ℓ for a distance of $10^4 \ell$. Figures 10(a,c) and 10(b,d) respectively show the PDFs of the principal stretches ϵ'_{ii} and shears ϵ'_{ij} for strongly heterogeneous ($\sigma_{lnK}^2 = 4$) Darcy flow for (a,b) fully anisotropic ($\delta = 1$) and (c,b) isotropic ($\delta = 0$) conductivity fields (5.1). For all flows computed the divergence error $|\sum_{i=1}^3 \epsilon'_{ii}| < 10^{-6}$ and the streamwise mean stretch $|\langle \epsilon'_{11}(t) \rangle| < 10^{-4}$ is also close to zero. For all flows the distributions of both ϵ'_{ii} and ϵ'_{ij} for $j > i$, $i = 1:3$ are broad and exhibit a sharp cutoff due to the finite nature of Ω . In all cases, the standard deviation is large $\sigma_{\epsilon'_{ii}} \gg |\langle \epsilon'_{ii} \rangle|$, however, the large number of independent observations (10^7) reduces the standard error to $\sigma_{\epsilon'_{ii}}/\sqrt{n} \sim 10^{-3}$, yielding accurate estimates of the principal stretches.

Figure 10(a,c) shows that the PDF of ϵ'_{11} is significantly broader for the isotropic case. This is attributed to the fact that in anisotropic media the local permeability varies with the local velocity orientation, leading to a narrower velocity distribution as the flow has a greater flexibility to minimise dissipation. The off-diagonal shears ϵ'_{ij} in figure 10(b,d) are all similarly distributed except the longitudinal shears ϵ'_{12} , ϵ'_{13} of the anisotropic flow are more broadly distributed as these streamlines are not confined to streamsurfaces and hence have higher curvature. The Protean transverse shear ϵ'_{23} in the isotropic case is zero as this is related to the helicity density as $\mathcal{H}(\mathbf{x}) = v'_i \epsilon_{ijk} \epsilon'_{jk} = v \epsilon'_{23}$ (Lester *et al.* 2018a).

For isotropic flow, the Lyapunov exponent is effectively zero ($|\langle \epsilon'_{ii} \rangle| < 10^{-4}$), whereas for anisotropic flow it is slightly larger than the theoretical upper bound $\lambda_\infty = \ln 2$, $(\langle \epsilon'_{11} \rangle, \langle \epsilon'_{22} \rangle, \langle \epsilon'_{33} \rangle) = (0.0001, 0.7148, -0.7149)$. The broad nature of the velocity gradient PDFs leads to a relatively large stretching variance, $\sigma_\lambda^2/\lambda_\infty \sim 10^2$ as shown in figure 8(d). This magnitude is consistent with the finding (discussed in § 3.1) that the ensemble average (3.3) $h = \lambda_\infty + \sigma^2/2$ is not correct, as this would not yield the agreement between h_{braid} and λ_∞ observed in figure 9(a). The broad distribution of all components of ϵ' has significant impacts upon the range of fluid processes hosted in these flows, as shall be explored further in § 6.

6. Implications of chaotic advection

The apparent ubiquity (based on the conjecture in § 4.2) of chaotic advection in heterogeneous and anisotropic Darcy flow has significant implications for the many fluidic

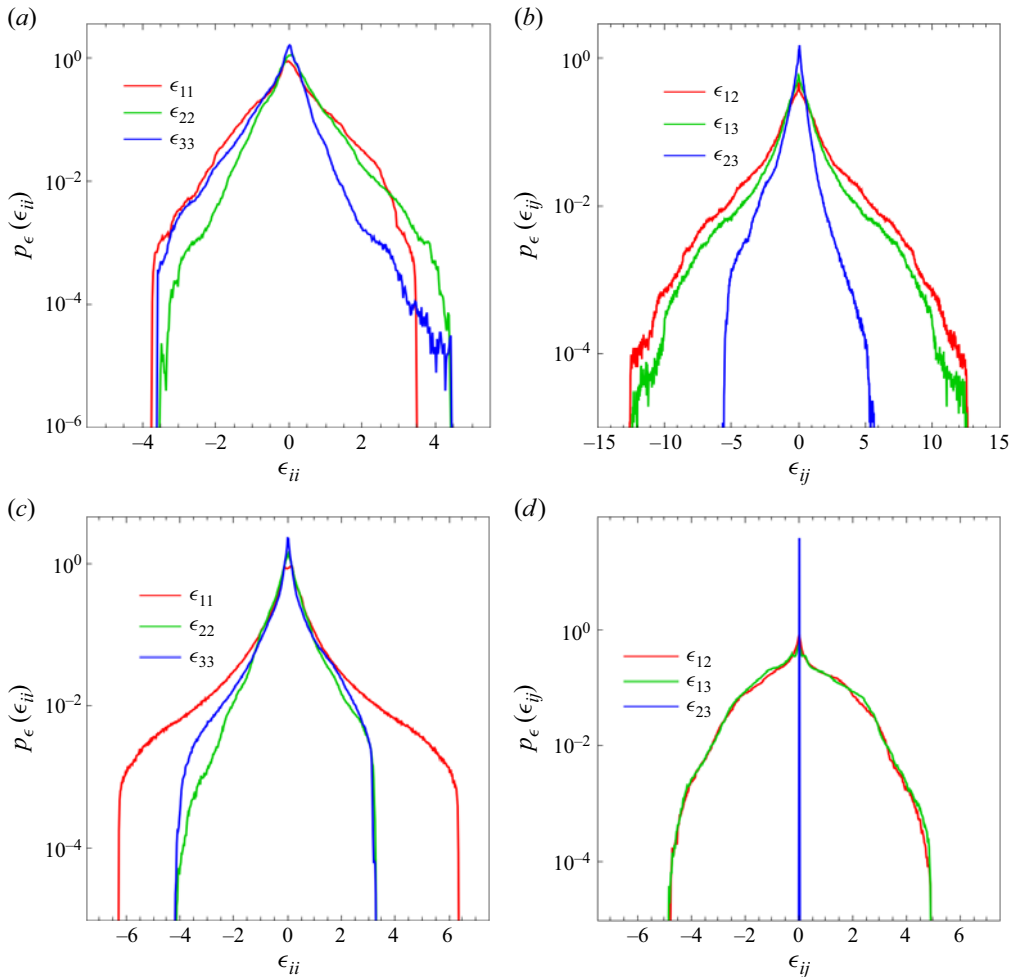


Figure 10. The PDFs of (a,c) diagonal ϵ_{ii} and (b,d) off-diagonal velocity gradient components ϵ_{ij} for (a,b) heterogeneous anisotropic Darcy flow (5.1) with $\sigma_{lnK}^2 = 4$, $\delta = 1$ and (c,d) isotropic Darcy flow (5.1) with $\sigma_{lnK}^2 = 4$, $\delta = 0$.

processes hosted in porous media, including transport and mixing of diffusive species such as solutes, colloids, reactive species and microorganisms. We briefly review these implications throughout this section. For these processes, the impact of chaotic dynamics scales with the Péclet number as \sqrt{Pe} (Aref *et al.* 2017), which can be large as Pe ranges from 10^{-1} to 10^7 in Darcy flows (Bear 1972; Delgado 2007).

Chaotic advection leads to qualitative changes in solute mixing and transport. Le Borgne *et al.* (2013) use a lamellar mixing model (Duplat & Villiermaux 2008) to show that in non-chaotic steady 2-D Darcy flow, the rate of mixing of diffusive solutes is governed by the rate of fluid deformation imparted by the medium heterogeneity. For 2-D (Dentz *et al.* 2016) and 3-D (Lester *et al.* 2021) isotropic Darcy flow, the rate of elongation $\rho(t) \equiv l(t)/l(0)$ of fluid elements grows algebraically as $\langle \rho(t) \rangle \sim t^r$, where the index $r = \mu + \nu$ varies from sublinear $r < 1$ to ballistic stretching $1 < r < 2$, depending upon the medium heterogeneity; μ , ν respectively characterise the mean and variance of the fluid stretching process. The lamellar mixing model (Le Borgne *et al.* 2013) predicts that the concentration

variance within the solute plume decays with time as

$$\langle c^2 \rangle \propto t^{-2\mu+2\nu+D_f+2}, \quad (6.1)$$

where D_f is the fractal dimension of material lines elongated by the flow. The lamellar mixing model also applies to turbulent and chaotic flows (Villermaux & Duplat 2003; Meunier & Villermaux 2010), yielding exponential decay of concentration variance as

$$\langle c^2 \rangle \propto \left(\frac{\lambda_\infty}{6t} \right)^{1/4} e^{-\lambda_\infty t/3}. \quad (6.2)$$

Hence, mixing of diffusive solutes is rapidly accelerated by chaotic advection. Similarly, the peak concentration $c_m(t)$ of a Gaussian plume which is inversely proportional to the dilution index $E(t) \equiv \exp[H(t)]$ (Kitanidis 1994) where $H(t)$ is the scalar entropy

$$H(t) = - \int_V d\mathbf{x} \frac{c(\mathbf{x}, t)}{\langle c \rangle} \ln \left[\frac{c(\mathbf{x}, t)}{\langle c \rangle} \right], \quad (6.3)$$

decays algebraically in non-chaotic heterogeneous porous media flow as (Dentz *et al.* 2018)

$$c_m(t) \propto \frac{1}{E(t)} \propto t^{-r}, \quad (6.4)$$

with $1 < r < 2$ (Dentz *et al.* 2016), whereas for chaotic flows these quantities evolve exponentially as

$$c_m(t) \propto \frac{1}{E(t)} \propto \exp(-\lambda_\infty t). \quad (6.5)$$

Hence, chaotic advection accelerates the rate of solute mixing from algebraic to exponential.

Chaotic advection also significantly enhances transverse dispersion. In the purely advective limit $Pe \rightarrow \infty$, transverse macro-dispersion coefficient $D_{T,\infty}$ is zero in non-chaotic Darcy flow, whereas for chaotic flow $D_{T,\infty} \sim \lambda_\infty^2$ as per (3.14). For diffusive solutes, D_T in non-chaotic Darcy flow is proportional to the transverse effective dispersion coefficient $D_{T,p}$ as (Lester *et al.* 2023)

$$D_T = D_{T,p} \langle m \rangle, \quad (6.6)$$

where $D_{T,p}$ accounts for pore-scale dispersion and m characterises fluctuations in streamlines due to heterogeneities in the conductivity field. A simple model of stretching-mediated dispersion around streamlines in chaotic Darcy flow that yields conservative dispersion estimates (see Appendix F for details) yields significantly larger transverse dispersion coefficient than (6.6)

$$D_T = D_{T,\infty} + D_{T,p} \frac{\sinh(2\lambda_\infty t_d)}{2\lambda_\infty t_d}, \quad (6.7)$$

where t_d is the period of stretching events.

Conversely, chaotic mixing suppresses longitudinal dispersion. Although results are not available for heterogeneous Darcy flow, studies of the impact of chaotic mixing on hold-up dispersion (Jones & Young 1994; Lester *et al.* 2018b) act as a guide for strongly heterogeneous media. For purely advective solutes, chaotic advection suppresses longitudinal variance from $\sigma_L^2(t) \sim t^2$ (Taylor 1953) for non-chaotic flows to $\sigma_L^2(t) \sim t^2/(\ln t)^3$ (Lester *et al.* 2010) due to increased sampling of advective velocities.

The impact of chaotic advection upon chemical reactions and biological activity is profound and multifaceted (Neufeld & Hernandez-Garcia 2009). For the simple case of fast binary reactions with Damköhler number $Da \rightarrow \infty$, the effective reaction kinetics are governed by solute mixing (Borgne, Ginn & Dentz 2014; Valocchi *et al.* 2019), hence the impacts outlined above for solute mixing directly translate to the rate and extent of these reactions. For simple binary reactions with finite Da , this acceleration becomes less pronounced with decreasing Da as the advective dynamics play less of a controlling role. Chaotic advection also has a profound impact upon more complex chemical, biological and geological reaction systems hosted in porous materials such as autocatalytic reactions, oscillatory reactions, bistable and competitive systems. Although these reaction systems converge toward a stable or stationary chemical state under well-mixed conditions, under incomplete mixing conditions – often found in porous materials (Wright, Richter & Bolster 2017) – transport of reactants can continually drive these systems away from local equilibrium (Neufeld & Hernandez-Garcia 2009). Hence, the accelerated transport characteristics inherent to chaotic advection can fundamentally alter the dynamics of these systems (Tél *et al.* 2005). Furthermore, the transport structures (LCS) generated by these flows lead to qualitatively different macroscopic behaviour including, e.g. singularly enhanced reactions and altered stability of competitive species (Károlyi *et al.* 2000).

7. Conclusions

The prevalence of chaotic advection in heterogeneous Darcy flow is a key consideration as these kinematics profoundly impact the myriad fluid-borne processes in porous media, ranging from solute mixing and transport to colloidal transport, chemical reactions and biological activity (Aref *et al.* 2017). In this study we directly address the question of the existence of chaotic advection for steady 3-D Darcy flow with smooth, finite hydraulic conductivity fields and find that chaotic advection is ubiquitous for all conductivity fields which are heterogeneous and anisotropic. We find that due to the absence of stagnation points in unbounded steady 3-D Darcy flow, all such flows have an embedded Hamiltonian structure (Ottino 1989), and so share many features with similar flows in the literature (Speetjens *et al.* 2021), including the transition to chaos from an integrable state.

We establish that realistic models of Darcy-scale heterogeneous porous media that admit transverse macro-dispersion in the large Péclet number limit, i.e. purely advective conditions should possess anisotropic hydraulic conductivity tensor fields $\mathbf{K}(\mathbf{x})$. A recently uncovered quantitative relationship (3.14) (Lester *et al.* 2024) between the purely advective transverse dispersion coefficient D_T and Lyapunov exponent λ_∞ in random unidirectional 3-dof flows also extends to steady 3-D Darcy flow. This establishes that transverse dispersion and chaotic advection in steady 3-D heterogeneous and anisotropic Darcy flow are intimately linked as both phenomena result from non-trivial streamline braiding, hence chaotic advection is inherent to these flows, subject to the conjecture regarding ergodicity of random flows discussed in § 4.2.

The onset of chaotic advection in steady 3-D Darcy flow is considered via numerical simulations of flow in two classes of hydraulic conductivity fields; heterogeneous fields with variable anisotropy, and anisotropic fields with variable heterogeneity. We find that chaotic advection arises even for the weakest perturbations away from both isotropic heterogeneous media and anisotropic homogeneous media, establishing that chaotic advection is inherent to anisotropic heterogeneous media. Simple relationships are found for how D_T and λ_∞ scale with medium anisotropy parameter δ and conductivity

log variance σ_{lnK}^2 , and excellent agreement is found with the theoretical model (3.14) linking D_T and λ_∞ in randomly braiding 3-dof flows. In the limit of large σ_{lnK}^2 , the Lyapunov exponent of anisotropic media converges to $\lambda_\infty \approx 0.6772$, which is close to the theoretical upper bound $\lambda_{\infty,max} = \ln 2 \approx 0.6931$ for 3-dof continuous systems, suggesting that anisotropic and highly heterogeneous Darcy flow is a strong mixing flow.

These results firmly establish the ubiquity of chaotic advection in steady 3-D anisotropic heterogeneous Darcy flow. We show that these kinematics have profound implications for understanding, quantifying and predicting a wide range of processes at the Darcy scale. The main finding of this study points to several future research directions. Further investigation of the quantitative link (3.14) between D_T and λ_∞ is required, as D_T has been measured for a wide range of porous materials (Zech *et al.* 2019), whereas λ_∞ has only been measured in a small number of studies (Kree & Villiermaux 2017; Souzy *et al.* 2020; Heyman *et al.* 2020, 2021) at the pore scale. Development of methods to characterise chaotic mixing at the field scale are required, as well as further investigation of the chaotic dynamics generated by geologically relevant conductivity fields, and fields that generate anomalous transport.

The results in figures 6(c) and 9(d) show that the dimensionless macro-dispersion coefficient $D_{T,m}/(\langle v \rangle \ell) \sim 10^{-1}$ in heterogeneous and anisotropic systems, which corresponds to transverse macro-dispersivity $\alpha_{T,m} = D_{T,m}/\langle v \rangle \sim \ell 10^{-1}$. As the correlation length scale ℓ ranges from order metres to kilometres in heterogeneous aquifers (Bear 1972), this is significantly greater than the pore-scale dispersivity $\alpha_{T,m}$ that is typically order millimetres (Gelhar 1986). These results also show that, consistent with field observations (Zech *et al.* 2019), the ratio of transverse to longitudinal to macro-dispersivity $\alpha_{T,m}/\alpha_{L,m} = D_{T,m}/D_{L,m}$ can vary significantly (from order $1-10^{-4}$ Zech *et al.* 2019), as longitudinal dispersivity $\alpha_{L,m}$ is controlled primarily by medium heterogeneity (Dentz *et al.* 2004), whereas transverse dispersivity is controlled by both medium heterogeneity and anisotropy. For highly anisotropic media $\alpha_{T,m}$ can be of similar magnitude to $\alpha_{L,m}$, whereas for isotropic media $\alpha_{T,m} \approx \alpha_{T,p}$ and so is significantly smaller than $\alpha_{L,m}$.

In the context of solute mixing and transport, further investigation and quantitative prediction of concentration PDF, transverse and longitudinal dispersion of diffusive solutes is required. Furthermore, the impact of chaotic mixing upon chemical reactions and biological activity in Darcy flow is an open area. The recognition that chaotic dynamics are inherent to porous media flow across all scales opens the door to the development of a broad class of upscaling methods that explicitly honour these kinematics and new class of tuneable engineered porous materials that exploit these phenomena. The ubiquity of macroscopic chaotic advection has profound implications for the myriad processes hosted in heterogeneous porous media, and calls for a fundamental re-evaluation of transport and reaction methods in macroscopic porous systems.

Acknowledgements. The authors gratefully acknowledge constructive comments from the anonymous reviewers which have led to improvements in this paper.

Funding. M.D. acknowledges funding by the European Union (ERC, KARST, 101071836). Views and opinions expressed are, however, those of the authors only, and do not necessarily reflect those of the European Union or the European Research Council Executive Agency. Neither the European Union nor the granting authority can be held responsible for them.

Declaration of interests. The authors report no conflict of interest.

Appendix A. Proof of zero total helicity H

We show that the total helicity H of conductivity fields of the form

$$\begin{aligned}\mathbf{K}(\mathbf{x}) &= \mathbf{K}_1(\mathbf{x}) + \mathbf{K}_2(\mathbf{x}), \\ &= k_0(\mathbf{x})\mathbf{I} + \delta k_0(\mathbf{x}) \hat{\mathbf{e}}_1 \otimes \hat{\mathbf{e}}_1,\end{aligned}\quad (\text{A1})$$

are zero (where $\delta \in [0, 1]$ controls the anisotropy of $\mathbf{K}(\mathbf{x})$) by expressing the corresponding velocity field as

$$\begin{aligned}\mathbf{v}(\mathbf{x}) &= -\mathbf{K}_1(\mathbf{x}) \cdot \nabla \phi - \mathbf{K}_2(\mathbf{x}) \cdot \nabla \phi, \\ &= \mathbf{v}_1(\mathbf{x}) + \mathbf{v}_2(\mathbf{x}),\end{aligned}\quad (\text{A2})$$

and thus the helicity density is

$$\begin{aligned}\mathcal{H}(\mathbf{x}) &= \mathbf{v}_1(\mathbf{x}) \cdot [\nabla \times \mathbf{v}_1(\mathbf{x})] + \mathbf{v}_2(\mathbf{x}) \cdot [\nabla \times \mathbf{v}_2(\mathbf{x})] \\ &\quad + \mathbf{v}_1(\mathbf{x}) \cdot [\nabla \times \mathbf{v}_2(\mathbf{x})] + \mathbf{v}_2(\mathbf{x}) \cdot [\nabla \times \mathbf{v}_1(\mathbf{x})],\end{aligned}\quad (\text{A3})$$

where the quantities on the top row of the RHS are zero. Expressing $\mathbf{v}_2(\mathbf{x}) = f(\mathbf{x})\hat{\mathbf{e}}_1$, then (A3) simplifies to

$$\begin{aligned}\mathcal{H}(\mathbf{x}) &= f(\mathbf{x}) \hat{\mathbf{e}}_1 \cdot [\nabla \times \mathbf{v}_1(\mathbf{x})] + \mathbf{v}_1(\mathbf{x}) \cdot [\nabla \times (f(\mathbf{x})\hat{\mathbf{e}}_1)] \\ &= \hat{\mathbf{e}}_1 \cdot [f(\mathbf{x})(\nabla \times \mathbf{v}_1(\mathbf{x}))] + \mathbf{v}_1(\mathbf{x}) \cdot [\nabla f(\mathbf{x}) \times \hat{\mathbf{e}}_1] \\ &= \hat{\mathbf{e}}_1 \cdot (\nabla \times [f(\mathbf{x})\mathbf{v}_1(\mathbf{x})]) \\ &= \nabla \cdot (x_1 \nabla \times [f(\mathbf{x})\mathbf{v}_1(\mathbf{x})]).\end{aligned}\quad (\text{A4})$$

Using the divergence theorem and continuity of $f(\mathbf{x})$ and $\mathbf{v}_1(\mathbf{x})$ over the periodic boundary $\partial\Omega$, the total helicity is zero

$$H = \int_{\Omega} \mathcal{H}(\mathbf{x}) \, d\mathbf{x} = \oint_{\partial\Omega} \mathbf{n} \cdot (x_1 \nabla \times [f(\mathbf{x})\mathbf{v}_1(\mathbf{x})]) = 0. \quad (\text{A5})$$

Appendix B. Fluid deformation in Protean coordinates

Fluid deformation is characterised by the deformation gradient tensor $\mathbf{F}(t; \mathbf{X})$ with Lagrangian coordinate \mathbf{X} , which evolves according to (3.15). The Lyapunov exponent and fluid stretching statistics are gathered by sampling ϵ along streamlines. The moving and rotating Protean coordinate frame provides several advantages as detailed in (Lester *et al.* 2018a) and briefly summarised as follows. The Protean coordinate frame \mathbf{x}' is related to the Eulerian frame \mathbf{x} as

$$\mathbf{x}'(t) = \mathbf{Q}(t) \cdot [\mathbf{x} - \mathbf{x}_0(t; \mathbf{X})], \quad (\text{B1})$$

where $\mathbf{x}_0(t; \mathbf{X})$ is the position of a fluid tracer particle at time t with initial position \mathbf{X} , and $\mathbf{Q}(t)$ is a time-dependent orthogonal rotation matrix. The Protean velocity gradient tensor $\epsilon'(t; \mathbf{X})$ is related to the Lagrangian velocity gradient tensor $\epsilon(t)$ as

$$\epsilon'(t; \mathbf{X}) = \mathbf{Q}^\top(t) \cdot \epsilon(t; \mathbf{X}) \cdot \mathbf{Q}(t) + \dot{\mathbf{Q}}^\top(t) \cdot \mathbf{Q}(t). \quad (\text{B2})$$

The rotational matrix $\mathbf{Q}(t)$ aligns the x'_1 coordinate with the local velocity direction such that $\hat{\mathbf{e}}'_1 = \mathbf{v}/v$, and for steady flow the Protean coordinate system is a streamline coordinate system. The rotation $\mathbf{Q}(t)$ comprises two subrotations as $\mathbf{Q}(t) = \mathbf{Q}_2(t) \cdot \mathbf{Q}_1(t)$, where the first rotation $\mathbf{Q}_1(t)$ aligns x'_1 with \mathbf{v}/v and so renders the ϵ'_{21} and ϵ'_{31} elements of the Protean velocity gradient tensor $\epsilon'(t; \mathbf{X})$ to be zero (Lester *et al.* 2018a). The second rotation $\mathbf{Q}_2(t)$ about the axis \mathbf{x}' in the streamwise direction is chosen such that the

remaining lower triangular element ϵ'_{23} is also zero (Lester *et al.* 2018a), rendering the Protean velocity gradient tensor upper triangular

$$\epsilon' = \begin{pmatrix} \epsilon'_{11} & \epsilon'_{12} & \epsilon'_{13} \\ 0 & \epsilon'_{22} & \epsilon'_{23} \\ 0 & 0 & \epsilon'_{33} \end{pmatrix}. \quad (\text{B3})$$

Hence, fluid deformation in the heterogeneous Darcy flows is characterised by computation of the Protean velocity gradient tensor along the streamlines of these flows.

Appendix C. Fluid stretching in 3-D Darcy flow

The 1-D CTRW (3.19) for evolution of $\rho(t; \mathbf{X})$ is derived by considering evolution of the infinitesimal line element $\delta \mathbf{l}(t; \mathbf{X}) = \mathbf{F}'(t; \mathbf{X}) \cdot \delta \mathbf{l}(0; \mathbf{X})$, the length of which evolves as

$$\delta l(t; \mathbf{X}) \equiv \|\delta \mathbf{l}(t; \mathbf{X})\| = \sqrt{\delta \mathbf{l}(0; \mathbf{X}) \cdot \mathbf{C}(t; \mathbf{X}) \cdot \delta \mathbf{l}(0; \mathbf{X})}, \quad (\text{C1})$$

where $\mathbf{C}(t; \mathbf{X}) = \mathbf{F}(t; \mathbf{X})^\top \cdot \mathbf{F}(t; \mathbf{X})$ is the symmetric Cauchy–Green tensor. Hence $\rho(t; \mathbf{X})$ grows with the largest eigenvalue $v(t; \mathbf{X})$ of $\mathbf{C}(t; \mathbf{X})$ as

$$\rho(t; \mathbf{X}) = \sqrt{v(t; \mathbf{X})}. \quad (\text{C2})$$

As detailed in § 3.4, the F'_{22} component characterises exponential stretching of fluid elements, and so converges to ρ (Lester *et al.* 2018a) in the asymptotic limit as

$$\lim_{t \rightarrow \infty} \frac{1}{t} \ln \rho(t; \mathbf{X}) = \lim_{t \rightarrow \infty} \frac{1}{2t} \ln v(t; \mathbf{X}) = \lim_{t \rightarrow \infty} \frac{1}{t} \ln F'_{22}(t; \mathbf{X}). \quad (\text{C3})$$

From (3.15), F'_{22} evolves with streamline distance s as

$$F'_{22,s}(s; \mathbf{X}) = \exp \left(\int_0^s \frac{\epsilon'_{22}(s'; \mathbf{X})}{v(s'; \mathbf{X})} ds' \right), \quad (\text{C4})$$

where $v(s; \mathbf{X}) = |\mathbf{v}(\mathbf{x}(s; \mathbf{X}))| = ds/dt$ is the local streamline velocity and $\mathbf{x}(s; \mathbf{X})$ is the position of a tracer particle along a streamline with initial position \mathbf{X} at $s = 0$, $t = 0$. As fluid velocity and velocity gradient are both spatially Markovian along streamlines (Le Borgne *et al.* 2008a; Lester *et al.* 2022), s may be discretised with respect to the spatial velocity correlation length ℓ as $s_n = n\ell$, with $n = 0, 1, \dots$, as per (3.19). Similarly, the advection time t_n and length stretch $\rho_n \equiv F'_{22,s}(s_n; \mathbf{X})$ at position s_n along a streamline evolves as per (3.19), with $v_n \equiv v(s_n; \mathbf{X})$, $\epsilon_n \equiv \epsilon'_{22}(s_n; \mathbf{X})$. Thus the CTRW (3.19) captures the line stretching dynamics in steady heterogeneous 3-D Darcy flow.

C.1. Fluid stretching under normal transport

Following (Dentz *et al.* 2016), from the CTRW (3.19), the Fourier–Laplace transform $\hat{p}_{\zeta,t}(k, \lambda)$ of the PDF $p_{\zeta,t}(\zeta, t)$ where λ is the Laplace variable for ζ and k is the Fourier variable for t is given by

$$\hat{p}_{\zeta,t}(k, \lambda) = \frac{1 - \hat{\psi}(\lambda)}{\lambda} \frac{1}{1 - \tilde{\psi}(k, \lambda)}, \quad (\text{C5})$$

where $\tilde{\psi}(k, \lambda)$ is given by

$$\tilde{\psi}(k, \lambda) = \hat{\psi}(\lambda) + \int_0^\infty dt \exp(-\lambda t) [\cos(|k|\epsilon t) - 1] \psi(t), \quad (\text{C6})$$

and $\hat{\psi}(\lambda)$ is the Laplace transform of $\psi(\tau)$, with τ the temporal increment defined in the CTRW (3.19). The moments of ζ are defined in terms of $\hat{p}_{\zeta,t}(k, \lambda)$ by

$$m_{j,\zeta} = (-i)^j \frac{\partial^j \hat{p}_{\zeta,t}(k, \lambda)}{\partial k^j} \Big|_{k=0}. \quad (\text{C7})$$

Hence

$$m_{1,\zeta} = 0, \quad m_{2,\zeta} = -\frac{1}{\lambda[1 - \hat{\psi}(\lambda)]} \frac{\partial^2 \tilde{\psi}(k, \lambda)}{\partial k^2} \Big|_{k=0}, \quad (\text{C8})$$

and the small k -expansion of (C6) is

$$\tilde{\psi}(k, \lambda) = \hat{\psi}(\lambda) - \int_0^\infty dt \exp(-\lambda t) \frac{1}{2} k^2 \sigma_\epsilon^2 t^2 \psi(t) + \dots, \quad (\text{C9})$$

and additional small λ -expansion

$$\tilde{\psi}(k, \lambda) = 1 - \frac{1}{2} k^2 \sigma_\epsilon^2 \langle \tau^2 \rangle + \dots \quad (\text{C10})$$

The small λ -expansion of $\hat{\psi}(\lambda)$ is

$$\hat{\psi}(\lambda) = 1 - \langle \tau \rangle \lambda + \frac{1}{2} \langle \tau^2 \rangle \lambda^2, \quad (\text{C11})$$

thus, we obtain to leading order

$$m_{2,\zeta} = \frac{\sigma_\epsilon^2 \langle \tau^2 \rangle}{\lambda^2 \langle \tau \rangle}, \quad (\text{C12})$$

the inverse Laplace transform of which gives

$$\lim_{t \rightarrow \infty} \sigma_{ln\rho}^2 = \sigma_\epsilon^2 \frac{\langle \tau^2 \rangle}{\langle \tau \rangle} t \equiv \sigma_\lambda^2 t. \quad (\text{C13})$$

Appendix D. Numerical solvers and streamline tracking

The potential fluctuation equation (5.4) for Darcy flow is solved to precision 10^{-16} on a uniform structured 256^3 grid using a high resolution eighth-order compact finite difference scheme (Lele 1992). To generate high resolution results and preserve the Lagrangian kinematics of the flow, we use a similar numerical approach to that used in (Lester *et al.* 2019). Specifically, we perform a triply periodic fifth-order spline interpolation of the primitive variables $\tilde{\phi}(\mathbf{x})$, $\mathbf{K}(\mathbf{x})$ from their grid values and reconstruct the potential field $\phi(\mathbf{x})$ according to (5.3). The velocity field is then computed analytically from these fields as $\mathbf{v}(\mathbf{x}) = -\mathbf{K}(\mathbf{x}) \cdot \nabla \phi(\mathbf{x})$, ensuring that the velocity field is triply periodic and C_4 continuous and the velocity gradient is accurately resolved for computation of fluid deformation in the Protean frame. This approach also implicitly enforces the helicity-free

constraint $h(\mathbf{x}) = 0$ for the case of isotropic conductivity tensor $\mathbf{K}(\mathbf{x}) = k(\mathbf{x})\mathbf{I}$ for $\delta = 0$. For the 256^3 mesh the local relative divergence error

$$d(\mathbf{x}) = \frac{|\nabla \cdot \mathbf{v}(\mathbf{x})|}{\|\nabla \mathbf{v}(\mathbf{x})\|}, \quad (\text{D1})$$

of the interpolated velocity field $\mathbf{v}(\mathbf{x})$ is order 10^{-4} and the velocity gradient is accurate to order 10^{-3} .

Streamline tracking is then computed by solving the advection equation from the initial Lagrangian coordinate \mathbf{X} as

$$\frac{d\mathbf{x}}{dt} = \mathbf{v}(\mathbf{x}(t; \mathbf{X})), \quad \mathbf{x}(0; \mathbf{X}) = \mathbf{X}, \quad (\text{D2})$$

via a fifth-order Cash–Karp Runge–Kutta scheme to precision 10^{-14} . The periodic boundaries allow advection of fluid streamlines over many multiples of the solution domain Ω , facilitating study of the Lagrangian kinematics over arbitrary distances. Although the corresponding velocity field is periodic in space, when the flow is chaotic the streamlines are aperiodic and eventually sample all of the conductivity field in an ergodic manner.

While accurate, this streamline tracking method (along with all numerical schemes which do not explicitly enforce kinematic constraints) has been shown (Lester *et al.* 2023) to introduce spurious transverse dispersion for the isotropic zero helicity density flow $h = 0$ due to numerical streamlines not following their analytic counterparts. To circumvent this problem for the helicity-free case $\delta = 0$, we instead solve the invariant streamfunctions $\psi_1(\mathbf{x})$, $\psi_2(\mathbf{x})$ for the velocity field $\mathbf{v}(\mathbf{x}) = \nabla\psi_1(\mathbf{x}) \times \nabla\psi_2(\mathbf{x})$ via the following governing equations (Lester *et al.* 2022) to precision 10^{-16} using the same finite-difference method as described above:

$$\nabla^2\psi_1(\mathbf{x}) - \nabla f(\mathbf{x}) \cdot \nabla\psi_1(\mathbf{x}) = S_1(\psi_1, \psi_2), \quad (\text{D3})$$

$$\nabla^2\psi_2(\mathbf{x}) - \nabla f(\mathbf{x}) \cdot \nabla\psi_2(\mathbf{x}) = S_2(\psi_1, \psi_2), \quad (\text{D4})$$

where $f = \ln k$ and

$$S_1 = \frac{(\mathbf{B} \times \psi_2) \cdot (\nabla\psi_1 \times \nabla\psi_2)}{|\nabla\psi_1 \times \nabla\psi_2|}, \quad S_2 = \frac{(\mathbf{B} \times \psi_1) \cdot (\nabla\psi_1 \times \nabla\psi_2)}{|\nabla\psi_1 \times \nabla\psi_2|}, \quad (\text{D5})$$

and

$$\mathbf{B} \equiv (\nabla\psi_1 \cdot \nabla)\nabla\psi_2 - (\nabla\psi_2 \cdot \nabla)\nabla\psi_1. \quad (\text{D6})$$

Similar to the Darcy equation, continuous streamfunctions $\psi_1(\mathbf{x})$, $\psi_2(\mathbf{x})$ are reconstructed from grid data using triply periodic splines and the velocity field is computed analytically from these streamfunctions. As shown in (Lester *et al.* 2022), this method yields the same velocity field (to within numerical error) as that given by direct solution of the Darcy equation.

Each family of streamfunctions ψ_i comprises a foliation of non-intersecting streamsurfaces $\psi_i = \text{const.}$ that span the flow domain and constrain the Lagrangian kinematics of the flow. This flow structure is non-chaotic as the advection equation (D2) simplifies to

$$\frac{ds}{dt} = v(s; \psi_1(\mathbf{X}), \psi_2(\mathbf{X})), \quad s(t = 0; \mathbf{X}) = 0, \quad (\text{D7})$$

where s is the distance travelled along a streamline of a tracer particle with initial position \mathbf{X} . The velocity magnitude $v(s; \psi_1(\mathbf{X}), \psi_2(\mathbf{X}))$ at the intersection of the

streamsurfaces $\psi_1(\mathbf{x}) = \psi_1(\mathbf{X})$, $\psi_2(\mathbf{x}) = \psi_2(\mathbf{X})$ only varies with s . Equation (D7) is integrable in that ψ_1, ψ_2 represent two invariants of the flow in the 3-D domain, resulting in only one degree of freedom (distance) for streamlines of the flow to explore. For helicity-free flow, we perform streamline tracking via numerical integration of (D7) to precision 10^{-8} . This approach ensures numerical streamlines follow their analytic counterparts and so enforces zero transverse dispersion and prevents the non-trivial braiding of streamlines that lead to chaotic advection.

Appendix E. Calculation of transverse dispersion coefficient

For both the variable anisotropy and variable heterogeneity Darcy flows, transverse dispersion coefficient is determined by tracking $N_p = 10^5$ streamlines over 10^3 traverses of the periodic domain Ω seeded from random locations within Ω . From these streamlines, the transverse variances are computed as

$$\sigma_{x_2}^2(t) = \frac{1}{N_p} \sum_{i=1}^{N_p} (x_{2,i}(t) - \langle x_2 \rangle(t))^2, \quad \langle x_2 \rangle(t) = \frac{1}{N_p} \sum_{i=1}^{N_p} x_{2,i}(t), \quad (\text{E1})$$

$$\sigma_{x_3}^2(t) = \frac{1}{N_p} \sum_{i=1}^{N_p} (x_{3,i}(t) - \langle x_3 \rangle(t))^2, \quad \langle x_3 \rangle(t) = \frac{1}{N_p} \sum_{i=1}^{N_p} x_{3,i}(t). \quad (\text{E2})$$

For the anisotropic Darcy flow with variable heterogeneity, the transverse variances exhibit slow growth and periodic oscillations in figure 11 for weak conductivity variance $\sigma_{lnK}^2 \ll 1$ as the streamlines of the flow are nearly periodic. With increasing heterogeneity σ_{lnK}^2 , these orbits lose periodicity and ergodically explore the flow domain, resulting in stronger growth of the transverse variances. The transverse dispersivities are related to the asymptotic variance growth as

$$D_{22} = \frac{1}{2} \lim_{t \rightarrow \infty} \frac{d\sigma_{x_2}^2}{dt}, \quad D_{33} = \frac{1}{2} \lim_{t \rightarrow \infty} \frac{d\sigma_{x_3}^2}{dt}. \quad (\text{E3})$$

To estimate this asymptotic growth we fit a linear function to the asymptotic variance data over two periods of the flow, as shown in figure 11. Note that the variance data in figure 11 has been truncated to 20 correlation lengths for illustrative purposes. The total transverse dispersion coefficient D_T is then computed as the average of the x_2 x_3 dispersivities.

Appendix F. Estimate of diffusive transverse dispersion coefficient

To generate a conservative estimate of diffusive transverse dispersion coefficient D_T under the action of chaotic advection, we consider a simple model for fluid deformation around at streamline at Lagrangian position \mathbf{X}_0 oriented in the $\mathbf{v}/v = \hat{\mathbf{e}}'_1$ direction of the Protean frame. Evolution of the local fluid deformation gradient tensor along the streamline is modelled via a ‘stretch and relax’ process over period t_d as

$$\mathbf{F}_0(t) = \begin{cases} \mathbf{F}_{00}(t) & \text{for } 0 < t \leq t_d, \\ \mathbf{F}_{00}(t_d - t) & \text{for } t_d < t \leq 2t_d, \end{cases} \quad (\text{F1})$$

and $\mathbf{F}_{00}(t) = \exp(\lambda_\infty t) \hat{\mathbf{e}}'_2 \otimes \hat{\mathbf{e}}'_2 + \exp(-\lambda_\infty t) \hat{\mathbf{e}}'_3 \otimes \hat{\mathbf{e}}'_3$ characterises the transverse stretching and contraction process. The deformation gradient tensor $\mathbf{F}(\mathbf{X}_0, t)$ on a streamline with Lagrangian coordinate \mathbf{X}_0 is then modelled as a series of sequential ‘stretch and

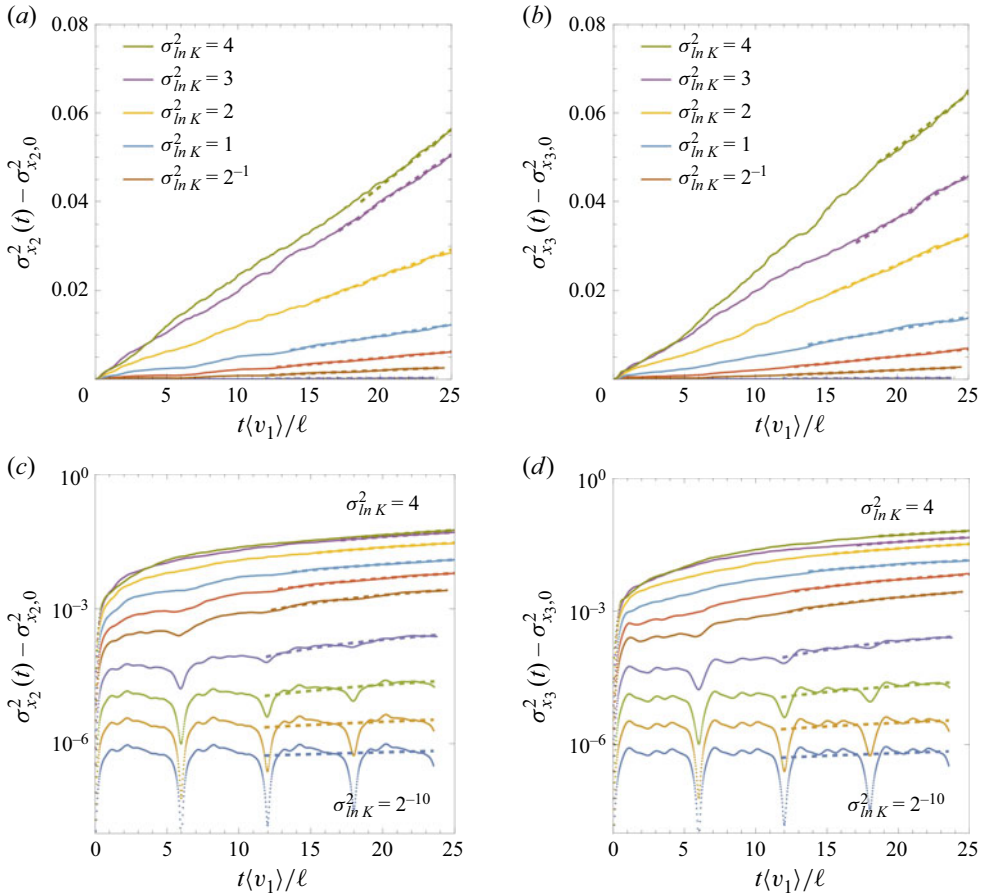


Figure 11. Evolution of transverse scalar variances $\sigma_{x_2}^2(t)$ (a,c), $\sigma_{x_3}^2(t)$ (b,d) with dimensionless travel time $t\langle v_1 \rangle / \ell$ in linear (a,b) and logarithmic (c,d) scales for heterogeneous anisotropic Darcy flow for various values of log variance $\sigma_{\ln K}^2$. Fitted linear trend (dashed lines) at late times is used to estimate transverse dispersivities D_{22} , D_{33} .

relax' processes with uniformly distributed random orientation $\theta \in [0, 2\pi]$ as

$$\mathbf{F}(\mathbf{X}, t) = [\mathbf{R}(\theta_n) \cdot \mathbf{F}_0(t) \cdot \mathbf{R}(\theta_n)^\top] \cdot \dots \cdot [\mathbf{R}(\theta_1) \cdot \mathbf{F}_0(2t_d) \cdot \mathbf{R}(\theta_1)^\top], \quad (\text{F2})$$

where $\mathbf{R}(\theta)$ is the rotation matrix around $\hat{\mathbf{e}}_1'$ and $n = \lceil t/(2t_d) \rceil$. This simple model generates a conservative estimate of dispersion as it does not capture persistent exponential stretching of fluid elements. However, such stretching in the absence of folding leads to erroneous predictions of transverse dispersion that grow exponentially in time. In practice, folding suppresses transverse dispersion to be sub-exponential, however, incorporation of such second-order deformation measures is beyond the scope of this model.

A solute packet centred about a streamline with Eulerian coordinate $\mathbf{x}_0(t) \equiv \mathbf{x}(\mathbf{X}_0, t)$ with initial concentration $c(\mathbf{x}, 0) = \delta(\mathbf{x} - \mathbf{x}_0)$ evolves with a Gaussian concentration profile

$$c(\mathbf{x}, t) = \frac{1}{\sqrt{(2\pi)^d \det \boldsymbol{\Sigma}(t)}} \exp \left(-\frac{1}{2} (\mathbf{x} - \mathbf{x}_0(t)) \cdot \boldsymbol{\Sigma}^{-1}(t) \cdot (\mathbf{x} - \mathbf{x}_0(t)) \right), \quad (\text{F3})$$

where the covariance matrix $\Sigma(t)$ evolves as (Dentz *et al.* 2018)

$$\Sigma(t) = 2D_{T,p} \mathbf{F}'(\mathbf{X}_0, t) \cdot \left(\int_0^t \mathbf{F}'(\mathbf{X}_0, t')^{-1} \cdot \mathbf{F}'(\mathbf{X}_0, t')^{-\top} dt' \right) \cdot \mathbf{F}'(\mathbf{X}_0, t)^{\top}, \quad (\text{F4})$$

which from (F2) simplifies to

$$\Sigma(2nt_d) = 2D_{T,p} \sum_{i=1}^n \mathbf{R}(\theta_n) \cdot \mathbf{A}_0 \cdot \mathbf{R}(\theta_n)^{\top}, \quad (\text{F5})$$

where

$$\mathbf{A}_0 = \frac{1 - e^{-2\hat{\lambda}_{\infty} t_d}}{\hat{\lambda}_{\infty}} \hat{\mathbf{e}}'_2 \otimes \hat{\mathbf{e}}'_2 + \frac{e^{2\hat{\lambda}_{\infty} t_d} - 1}{\hat{\lambda}_{\infty}} \hat{\mathbf{e}}'_2 \otimes \hat{\mathbf{e}}'_2. \quad (\text{F6})$$

Hence, for large t , the covariance matrix converges to $\Sigma(t) = 2D_{T,p} n \langle \mathbf{A} \rangle$ where

$$\langle \mathbf{A} \rangle \equiv \frac{1}{2\pi} \int_0^{2\pi} [\mathbf{R}(\theta) \cdot \mathbf{A}_0 \cdot \mathbf{R}(\theta)^{\top}] d\theta, \quad (\text{F7})$$

and so

$$\Sigma(t) = 2D_{T,p} t \frac{\sinh(2\hat{\lambda}_{\infty} t_d)}{2\hat{\lambda}_{\infty} t_d} \mathbf{1}. \quad (\text{F8})$$

Hence, macroscopic transverse dispersion around streamlines is exponentially amplified by periodic stretching. In conjunction with advective dispersion of streamlines, this yields (6.7). Note that similar to (6.6), this model is only valid for $\|\Sigma(t)\| < \ell$.

REFERENCES

- ALONSO-MATILLA, R., CHAKRABARTI, B. & SAINTILLAN, D. 2019 Transport and dispersion of active particles in periodic porous media. *Phys. Rev. Fluids* **4** (4), 043101.
- ANNA, P.D., JIMENEZ-MARTINEZ, J., TABUTEAU, H., TURUBAN, R., LE BORGNE, T., DERRIEN, M. & MÉHEUST, Y. 2013 Mixing and reaction kinetics in porous media: an experimental pore scale quantification. *Environ. Sci. Technol.* **48** (1), 508–516.
- AQUINO, T., LE BORGNE, T. & HEYMAN, J. 2023 Fluid–solid reaction in porous media as a chaotic restart process. *Phys. Rev. Lett.* **130**, 264001.
- AREF, H. 1984 Stirring by chaotic advection. *J. Fluid Mech.* **143**, 1–21.
- AREF, H. 2017 Frontiers of chaotic advection. *Rev. Mod. Phys.* **89** (2), 025007.
- ARNOL'D, V.I. 1965 Sur la topologie des écoulements stationnaires des fluides parfaits. *Comptes Rendus Acad. Sci. Paris* **261**, 312–314.
- ARTIN, E. 1947 Theory of braids. *Ann. Maths* **48**, 101–126.
- BAJER, K. 1994 Hamiltonian formulation of the equations of streamlines in three-dimensional steady flows. *Chaos Solitons Fract.* **4** (6), 895–911.
- BEAR, J. 1972 Dynamics of fluids in porous media. In *Dover Classics of Science and Mathematics*, vol. 1, pp. 1–617. Dover.
- BEAUDOIN, A. & DE DREUZY, J.-R. 2013 Numerical assessment of 3-D macrodispersion in heterogeneous porous media. *Water Resour. Res.* **49** (5), 2489–2496.
- BERKOWITZ, B., CORTIS, A., DENTZ, M. & SCHER, H. 2006 Modeling non-Fickian transport in geological formations as a continuous time random walk. *Rev. Geophys.* **44** (2), RG2003.
- BIJELJIC, B. & BLUNT, M.J. 2006 Pore-scale modeling and continuous time random walk analysis of dispersion in porous media. *Water Resour. Res.* **42**, W01202.
- BIJELJIC, B. & BLUNT, M.J. 2007 Pore-scale modeling of transverse dispersion in porous media. *Water Resour. Res.* **43** (12), W12S11.
- BOON, M., BIJELJIC, B., NIU, B. & KREVOR, S. 2016 Observations of 3-D transverse dispersion and dilution in natural consolidated rock by X-ray tomography. *Adv. Water Resour.* **96**, 266–281.
- BOOZER, A.H. 2005 Physics of magnetically confined plasmas. *Rev. Mod. Phys.* **76**, 1071–1141.

- BOYLAND, P.L., AREF, H. & STREMLER, M.A. 2000 Topological fluid mechanics of stirring. *J. Fluid Mech.* **403**, 277–304.
- BRENNER, H. & EDWARDS, D. 1993 *Macrotransport Processes*. Butterworth–Heinemann.
- BROUWER, L.E.J. 1911 Über abbildung von mannigfaltigkeiten. *Math. Ann.* **71** (1), 97–115.
- BUDIŠIĆ, M. & THIFFEAULT, J.-L. 2015 Finite-time braiding exponents. *Chaos: Interdisciplinary J. Nonlinear Sci.* **25** (8), 087407.
- CATALAN, T. 2019 A link between topological entropy and Lyapunov exponents. *Ergod. Theor. Dyn. Syst.* **39** (3), 620–637.
- CERBELLI, S., GIONA, M., GORODETSKYI, O. & ANDERSON, P.D. 2017 Singular eigenvalue limit of advection-diffusion operators and properties of the strange eigenfunctions in globally chaotic flows. *Eur. Phys. J. Special Topics* **226** (10), 2247–2262.
- CHAUDHURI, A. & SEKHAR, M. 2005 Analytical solutions for macrodispersion in a 3D heterogeneous porous medium with random hydraulic conductivity and dispersivity. *Transp. Porous Med.* **58** (3), 217–241.
- CHIOGNA, G., ROLLE, M., BELLIN, A. & CIRPKA, O.A. 2014 Helicity and flow topology in three-dimensional anisotropic porous media. *Adv. Water Resour.* **73**, 134–143.
- CHO, M.S., SOLANO, F., THOMSON, N.R., TREFRY, M.G., LESTER, D.R. & METCALFE, G. 2019 Field trials of chaotic advection to enhance reagent delivery. *Groundwater Monitoring Remediation* **39** (3), 23–39.
- CIRPKA, O.A., CHIOGNA, G., ROLLE, M. & BELLIN, A. 2015 Transverse mixing in three-dimensional nonstationary anisotropic heterogeneous porous media. *Water Resour. Res.* **51** (1), 241–260.
- COCKE, W.J. 1969 Turbulent hydrodynamic line stretching: consequences of isotropy. *Phys. Fluids* **12** (12), 2488–2492.
- CUSHMAN, J.H. 2013 *The Physics of Fluids in Hierarchical Porous Media: Angstroms to Miles*, vol. 10. Springer Science & Business Media.
- DAGAN, G. 1987 Theory of solute transport by groundwater. *Annu. Rev. Fluid Mech.* **19** (1), 183–213.
- DAGAN, G. 1989 *Flow and Transport in Porous Formations*. Springer.
- DARTOIS, A., BEAUDOIN, A. & HUBERSON, S. 2018 Impact of local diffusion on macroscopic dispersion in three-dimensional porous media. *Comptes Rendus Mécanique* **346** (2), 89–97.
- DELGADO, J.M.P.Q. 2007 Longitudinal and transverse dispersion in porous media. *Chem. Engng Res. Des.* **85** (9), 1245–1252.
- DENTZ, M., DE BARROS, F.P.J., LE BORGNE, T. & LESTER, D.R. 2018 Evolution of solute blobs in heterogeneous porous media. *J. Fluid Mech.* **853**, 621–646.
- DENTZ, M., CORTIS, A., SCHER, H. & BERKOWITZ, B. 2004 Time behavior of solute transport in heterogeneous media: transition from anomalous to normal transport. *Adv. Water Resour.* **27** (2), 155–173.
- DENTZ, M., CREPPY, A., DOUARCHE, C., CLÉMENT, E. & AURADOU, H. 2022 Dispersion of motile bacteria in a porous medium. *J. Fluid Mech.* **946**, A33.
- DENTZ, M., HIDALGO, J.J. & LESTER, D. 2023 Mixing in porous media: concepts and approaches across scales. *Transp. Porous Med.* **146** (1), 5–53.
- DENTZ, M., LE BORGNE, T., LESTER, D.R. & DE BARROS, F.P.J. 2015 Scaling forms of particle densities for Lévy walks and strong anomalous diffusion. *Phys. Rev. E* **92**, 032128.
- DENTZ, M., LESTER, D.R., LE BORGNE, T. & DE BARROS, F.P.J. 2016 Coupled continuous-time random walks for fluid stretching in two-dimensional heterogeneous media. *Phys. Rev. E* **94**, 061102.
- DINH, T.-C. & SIBONY, N. 2008 Upper bound for the topological entropy of a meromorphic correspondence. *Isr. J. Math.* **163** (1), 29–44.
- DUPLAT, J., INNOCENTI, C. & VILLERMAUX, E. 2010 A nonsequential turbulent mixing process. *Phys. Fluids* **22** (3), 035104.
- DUPLAT, J. & VILLERMAUX, E. 2008 Mixing by random stirring in confined mixtures. *J. Fluid Mech.* **617**, 51–86.
- FEREDAY, D.R. & HAYNES, P.H. 2004 Scalar decay in two-dimensional chaotic advection and Batchelor-regime turbulence. *Phys. Fluids* **16** (12), 4359–4370.
- FINN, M.D. & THIFFEAULT, J.-L. 2007 Topological entropy of braids on the torus. *SIAM J. Appl. Dyn. Syst.* **6** (1), 79–98.
- GELHAR, L.W. 1986 Stochastic subsurface hydrology from theory to applications. *Water Resour. Res.* **22** (9S), 135S–145S.
- GELHAR, L.W. & AXNESS, C.L. 1983 Three-dimensional stochastic analysis of macrodispersion in aquifers. *Water Resour. Res.* **19** (1), 161–180.
- GIRIMAJI, S.S. & POPE, S.B. 1990 Material-element deformation in isotropic turbulence. *J. Fluid Mech.* **220**, 427–458.
- HAKOUN, V., COMOLLI, A. & DENTZ, M. 2019 Upscaling and prediction of Lagrangian velocity dynamics in heterogeneous porous media. *Water Resour. Res.* **55** (5), 3976–3996.

- HALL, T. & YURTTAŞ, S.Ö. 2009 On the topological entropy of families of braids. *Topol. Applics.* **156** (8), 1554–1564.
- HALLER, G. 2015 Lagrangian coherent structures. *Annu. Rev. Fluid Mech.* **47** (2015), 137–162.
- HALLER, G. & POJE, A.C. 1998 Finite time transport in aperiodic flows. *Physica D: Nonlinear Phenom.* **119** (3–4), 352–380.
- HALLER, G. & SAPSIS, T. 2008 Where do inertial particles go in fluid flows? *Physica D: Nonlinear Phenom.* **237** (5), 573–583.
- HANDEL, M. & THURSTON, W.P. 1985 New proofs of some results of Nielsen. *Adv. Math.* **56** (2), 173–191.
- HESS, K.M., WOLF, S.H. & CELIA, M.A. 1992 Large-scale natural gradient tracer test in sand and gravel, Cape Cod, Massachusetts: 3. Hydraulic conductivity variability and calculated macrodispersivities. *Water Resour. Res.* **28** (8), 2011–2027.
- HEYMAN, J., LESTER, D.R. & LE BORGNE, T. 2021 Scalar signatures of chaotic mixing in porous media. *Phys. Rev. Lett.* **126**, 034505.
- HEYMAN, J., LESTER, D.R., TURUBAN, R., MÉHEUST, Y. & LE BORGNE, T. 2020 Stretching and folding sustain microscale chemical gradients in porous media. *Proc. Natl Acad. Sci. USA* **117** (24), 13359–13365.
- HINCH, E.J. 1999 *Mixing: Turbulence and Chaos – An Introduction*. Springer US.
- HOBBS, D.M. & MUZZIO, F.J. 1997 The Kenics static mixer: a three-dimensional chaotic flow. *Chem. Engng J.* **67** (3), 153–166.
- HOLM, D.D. & KIMURA, Y. 1991 Zero-helicity Lagrangian kinematics of three-dimensional advection. *Phys. Fluids A: Fluid Dyn.* **3** (5), 1033–1038.
- JANKOVIĆ, I., STEWARD, D.R., BARNES, R. J. & DAGAN, G. 2009 Is transverse macrodispersivity in three-dimensional groundwater transport equal to zero? A counterexample. *Water Resour. Res.* **45** (8), W08415.
- JONES, S.W. & YOUNG, W.R. 1994 Shear dispersion and anomalous diffusion by chaotic advection. *J. Fluid Mech.* **280**, 149–172.
- KALDA, J. 2000 Simple model of intermittent passive scalar turbulence. *Phys. Rev. Lett.* **84**, 471–474.
- KANG, T.G., SINGH, M.K., KWON, T.H. & ANDERSON, P.D. 2008 Chaotic mixing using periodic and aperiodic sequences of mixing protocols in a micromixer. *Microfluid Nanofluid* **4** (6), 589–599.
- KÁROLYI, G., PÉNTEK, Á., SCHEURING, I., TÉL, T. & TOROČZKAI, Z. 2000 Chaotic flow: the physics of species coexistence. *Proc. Natl Acad. Sci.* **97** (25), 13661–13665.
- KATOK, A. & HASSELBLATT, B. 1995 *Introduction to the Modern Theory of Dynamical Systems. Encyclopedia of Mathematics and its Applications 1*. Cambridge University Press.
- KITANIDIS, P.K. 1994 The concept of the dilution index. *Water Resour. Res.* **30**, 2011–2026.
- KREE, M. & VILLERMAUX, E. 2017 Scalar mixtures in porous media. *Phys. Rev. Fluids* **2**, 104502.
- LE BORGNE, T., DENTZ, M. & CARRERA, J. 2008a Lagrangian statistical model for transport in highly heterogeneous velocity fields. *Phys. Rev. Lett.* **101**, 090601.
- LE BORGNE, T., DENTZ, M. & CARRERA, J. 2008b Spatial Markov processes for modeling Lagrangian particle dynamics in heterogeneous porous media. *Phys. Rev. E* **78**, 026308.
- LE BORGNE, T., DENTZ, M. & VILLERMAUX, E. 2013 Stretching, coalescence, and mixing in porous media. *Phys. Rev. Lett.* **110**, 204501.
- LE BORGNE, T., DENTZ, M. & VILLERMAUX, E. 2015 The lamellar description of mixing in porous media. *J. Fluid Mech.* **770**, 458–498.
- BORGNE, T.L., GINN, T.R. & DENTZ, M. 2014 Impact of fluid deformation on mixing-induced chemical reactions in heterogeneous flows. *Geophys. Res. Lett.* **41** (22), 7898–7906.
- LELE, S.K. 1992 Compact finite difference schemes with spectral-like resolution. *J. Comput. Phys.* **103**, 16–42.
- LESTER, D.R., TREFRY, M.G. & METCALFE, G. 2016a Chaotic advection at the pore scale: mechanisms, upscaling and implications for macroscopic transport. *Adv. Water Resour.* **97**, 175–192.
- LESTER, D.R., BANDOPADHYAY, A., DENTZ, M. & LE BORGNE, T. 2019 Hydrodynamic dispersion and lamb surfaces in Darcy flow. *Transp. Porous Med.* **130** (3), 903–922.
- LESTER, D.R. & DENTZ, M. 2025 Line stretching in random flows. [arXiv:2504.17982](https://arxiv.org/abs/2504.17982).
- LESTER, D.R., DENTZ, M., BANDOPADHYAY, A. & LE BORGNE, T. 2022 Fluid deformation in isotropic Darcy flow. *J. Fluid Mech.* **945**, A18.
- LESTER, D.R., DENTZ, M., BANDOPADHYAY, A. & LE BORGNE, T. 2021 The Lagrangian kinematics of three-dimensional Darcy flow. *J. Fluid Mech.* **918**, A27.
- LESTER, D.R., DENTZ, M., LE BORGNE, T. & DE BARROS, F.P.J. 2018a Fluid deformation in random steady three-dimensional flow. *J. Fluid Mech.* **855**, 770–803.
- LESTER, D.R., DENTZ, M. & LE BORGNE, T. 2016b Chaotic mixing in three-dimensional porous media. *J. Fluid Mech.* **803**, 144–174.
- LESTER, D.R., DENTZ, M., SINGH, P. & BANDOPADHYAY, A. 2023 Under what conditions does transverse macrodispersion exist in groundwater flow? *Water Resour. Res.* **59** (3), e2022WR033059.

- LESTER, D.R., KUAN, B. & METCALFE, G. 2018*b* Simultaneous optimisation of residence time, heat and mass transfer in laminar duct flows. *Chem. Engng Sci.* **191**, 511–524.
- LESTER, D.R., METCALFE, G. & TREFRY, M.G. 2013 Is chaotic advection inherent to porous media flow? *Phys. Rev. Lett.* **111**, 174101.
- LESTER, D.R., METCALFE, G. & TREFRY, M.G. 2014 Anomalous transport and chaotic advection in homogeneous porous media. *Phys. Rev. E* **90**, 063012.
- LESTER, D.R., METCALFE, G. & TREFRY, M.G. 2024 Braiding flows link stirring and dispersion, [arXiv:2412.05407](https://arxiv.org/abs/2412.05407).
- LESTER, D.R., RUDMAN, M., METCALFE, G., TREFRY, M.G., ORD, A. & HOBBS, B. 2010 Scalar dispersion in a periodically reoriented potential flow: acceleration via Lagrangian chaos. *Phys. Rev. E* **81**, 046319.
- LIU, M., MUZZIO, F.J. & PESKIN, R.L. 1994 Quantification of mixing in aperiodic chaotic flows. *Chaos Solitons Fract.* **4** (6), 869–893.
- LIU, Y., XIAO, H., AQUINO, T., DENTZ, M. & WANG, M. 2024 Scaling laws and mechanisms of hydrodynamic dispersion in porous media. *J. Fluid Mech.* **1001**, R2.
- MATSUOKA, C. & HIRAIDE, K. 2015 Computation of entropy and Lyapunov exponent by a shift transform. *Chaos: Interdisciplinary J. Nonlinear Sci.* **25** (10), 103110.
- MAYS, D.C. & NEUPAUER, R.M. 2012 Plume spreading in groundwater by stretching and folding. *Water Resour. Res.* **48** (7), W07501.
- METCALFE, G., LESTER, D., ORD, A., KULKARNI, P., TREFRY, M., HOBBS, B.E., REGENAUR-LIEB, K. & MORRIS, J. 2010 A partially open porous media flow with chaotic advection: towards a model of coupled fields. *Phil. Trans. R. Soc. A: Math. Phys. Engng Sci.* **368** (1910), 217–230.
- METCALFE, G., LESTER, D. & TREFRY, M. 2023 A primer on the dynamical systems approach to transport in porous media. *Transp. Porous Med.* **146** (1), 55–84.
- METCALFE, G., RUDMAN, M., BRYDON, A., GRAHAM, L.J.W. & HAMILTON, R. 2006 Composing chaos: an experimental and numerical study of an open duct mixing flow. *AIChE J.* **52** (1), 9–28.
- MEUNIER, P. & VILLERMAUX, E. 2010 The diffusive strip method for scalar mixing in two dimensions. *J. Fluid Mech.* **662**, 134–172.
- MOFFATT, H.K. 1969 The degree of knottedness of tangled vortex lines. *J. Fluid Mech.* **1**, 117–129.
- MOFFATT, H.K. & TSINOBER, A. 1992 Helicity in laminar and turbulent flow. *Annu. Rev. Fluid Mech.* **24** (1), 281–312.
- MOREAU, J.J. 1961 Constantes d'un flot tourbillonnaire en fluide parfait barotrope. *Comptes Rendus Acad. Sci. Paris* **252**, 2810–2812.
- MOUSSAFIR, J.-O. 2006 On computing the entropy of braids. *Funct. Anal. Other Maths* **1** (1), 37–46.
- NEUFELD, Z. & HERNANDEZ-GARCIA, E. 2009 *Chemical and Biological Processes in Fluid Flows: A Dynamical Systems Approach*. Imperial College Press.
- NEUMAN, S.P. & ZHANG, Y.-K. 1990 A quasi-linear theory of non-Fickian and Fickian subsurface dispersion: 1. theoretical analysis with application to isotropic media. *Water Resour. Res.* **26** (5), 887–902.
- NEWHOUSE, S. & PIGNATARO, T. 1993 On the estimation of topological entropy. *J. Stat. Phys.* **72** (5), 1331–1351.
- NEWHOUSE, S.E. 1988 Entropy and volume. *Ergod. Theory Dyn. Sys.* **8**, 283–299.
- ÓDOR, G. 2004 Universality classes in nonequilibrium lattice systems. *Rev. Mod. Phys.* **76**, 663–724.
- ONU, K., HUHN, F. & HALLER, G. 2015 LCS tool: a computational platform for Lagrangian coherent structures. *J. Comput. Sci.* **7**, 26–36.
- OTTINO, J.M. 1989 *The Kinematics of Mixing: Stretching, Chaos, and Transport*. Cambridge University Press.
- OUELLETTE, N.T., O'MALLEY, P.J.J. & GOLLUB, J.P. 2008 Transport of finite-sized particles in chaotic flow. *Phys. Rev. Lett.* **101** (17), 174504.
- POJE, A.C., HALLER, G. & MEZIĆ, I. 1999 The geometry and statistics of mixing in aperiodic flows. *Phys. Fluids* **11** (10), 2963–2968.
- PUYGUIRAUD, A., GOUZE, P. & DENTZ, M. 2021 Pore-scale mixing and the evolution of hydrodynamic dispersion in porous media. *Phys. Rev. Lett.* **126**, 164501.
- RAJARAM, H. & GELHAR, L.W. 1991 Three-dimensional spatial moments analysis of the borden tracer test. *Water Resour. Res.* **27** (6), 1239–1251.
- REBENSHTOK, A., DENISOV, S., HÄNGGI, P. & BARKAI, E. 2014 Non-normalizable densities in strong anomalous diffusion: beyond the central limit theorem. *Phys. Rev. Lett.* **112**, 110601.
- RENARD, P. & DE MARSILY, G. 1997 Calculating equivalent permeability: a review. *Adv. Water Resour.* **20** (5–6), 253–278.
- ROBERTS, E., SINDI, S., SMITH, S.A. & MITCHELL, K.A. 2019 Ensemble-based topological entropy calculation (E-tec). *Chaos: Interdisciplinary J. Nonlinear Sci.* **29** (1), 013124.
- ROLLE, M. & LE BORGNE, T. 2019 Mixing and reactive fronts in the subsurface. *Rev. Mineral. Geochem.* **85** (1), 111–142.

- SAFFMAN, P.G. 1959 A theory of dispersion in a porous medium. *J. Fluid Mech.* **6** (3), 321–349.
- SCHUTZ, B.F. 1980 *Geometrical Methods of Mathematical Physics*. Cambridge University Press.
- SOUZY, M., LHUISSIER, H., MÉHEUST, Y., LE BORGNE, T. & METZGER, B. 2020 Velocity distributions, dispersion and stretching in three-dimensional porous media. *J. Fluid Mech.* **891**, A16.
- SPEETJENS, M., METCALFE, G. & RUDMAN, M. 2006 Topological mixing study of non-Newtonian duct flows. *Phys. Fluids* **18** (10), 103103.
- SPEETJENS, M., METCALFE, G. & RUDMAN, M. 2021 Lagrangian transport and chaotic advection in three-dimensional laminar flows. *Appl. Mech. Rev.* **73** (3), 030801.
- SQUIRES, T.M. & QUAKE, S.R. 2005 Microfluidics: fluid physics at the nanoliter scale. *Rev. Mod. Phys.* **77**, 977–1026.
- STONE, H.A., STROOCK, A.D. & AJDARI, A. 2004 Engineering flows in small devices: microfluidics toward a lab-on-a-chip. *Annu. Rev. Fluid Mech.* **36**, 381–411.
- STROOCK, A.D., DERTINGER, S.K.W., AJDARI, A., MEZIĆ, I., STONE, H.A. & WHITESIDES, G.M. 2002 Chaotic mixer for microchannels. *Science* **295** (5555), 647–651.
- SUDICKY, E.A., CHERRY, J.A. & FRIND, E.O. 1983 Migration of contaminants in groundwater at a landfill: a case study: 4. A natural-gradient dispersion test. *J. Hydrol.* **63** (1), 81–108.
- SURANA, A., GRUNBERG, O. & HALLER, G. 2006 Exact theory of three-dimensional flow separation. Part 1. Steady separation. *J. Fluid Mech.* **564**, 57–103.
- TAYLOR, G.I. 1953 Dispersion of soluble matter in solvent flowing slowly through a tube. *Phil. Trans. R. Soc. A: Math. Phys. Engng Sci.* **219**, 186–203.
- TÉL, T., KÁROLYI, G., PÉNTEK, Á., SCHEURING, I., TOROCZKAI, Z., GREBOGI, C. & KADTKE, J. 2000 Chaotic advection, diffusion, and reactions in open flows. *Chaos: Interdisciplinary J. Nonlinear Sci.* **10** (1), 89–98.
- TÉL, T., DE MOURA, A., GREBOGI, C. & KÁROLYI, G. 2005 Chemical and biological activity in open flows: a dynamical system approach. *Phys. Rep.* **413** (2–3), 91–196.
- THIFFEAULT, J.-L. 2005 Measuring topological chaos. *Phys. Rev. Lett.* **94**, 084502.
- THIFFEAULT, J.-L. 2010 Braids of entangled particle trajectories. *Chaos: Interdisciplinary J. Nonlinear Sci.* **20** (1), 017516.
- THIFFEAULT, J.-L. 2022 *Braids and Dynamics*. Springer Cham.
- THIFFEAULT, J.-L. & BUDIŠIĆ, M. 2013–2021 Braidlab: a software package for braids and loops, version 3.2.5. [arXiv:1410.0849](https://arxiv.org/abs/1410.0849) [math.GT]
- THIFFEAULT, J.-L. & FINN, M.D. 2006 Topology, braids and mixing in fluids. *Phil. Trans. R. Soc. A: Math. Phys. Engng Sci.* **364**, 3251–3266.
- TREFRY, M.G., LESTER, D.R., METCALFE, G. & WU, J. 2019 Temporal fluctuations and poroelasticity can generate chaotic advection in natural groundwater systems. *Water Resour. Res.* **55** (4), 3347–3374.
- TURUBAN, R., LESTER, D.R., HEYMAN, J., BORGNE, T.L. & MÉHEUST, Y. 2019 Chaotic mixing in crystalline granular media. *J. Fluid Mech.* **871**, 562–594.
- TURUBAN, R., LESTER, D.R., LE BORGNE, T. & MÉHEUST, Y. 2018 Space-group symmetries generate chaotic fluid advection in crystalline granular media. *Phys. Rev. Lett.* **120** (2), 024501.
- VALOCCHI, A.J., BOLSTER, D. & WERTH, C.J. 2019 Mixing-limited reactions in porous media. *Transp. Porous Med.* **130** (1), 157–182.
- VÉTEL, J., GARON, A. & PELLETIER, D. 2009 Lagrangian coherent structures in the human carotid artery bifurcation. *Exp. Fluids* **46** (6), 1067–1079.
- VILLERMAUX, E. 2012 Mixing by porous media. *Comptes Rendus Mécanique* **340** (11–12), 933–943.
- VILLERMAUX, E. 2019 Mixing versus stirring. *Annu. Rev. Fluid Mech.* **51** (1), 245–273.
- VILLERMAUX, E. & DUPLAT, J. 2003 Mixing as an aggregation process. *Phys. Rev. Lett.* **91**, 184501.
- WOLTIER, L. 1958 A theorem on force-free magnetic fields. *Proc. Natl Acad. Sci. USA* **44** (6), 489–491.
- WRIGHT, E.E., RICHTER, D.H. & BOLSTER, D. 2017 Effects of incomplete mixing on reactive transport in flows through heterogeneous porous media. *Phys. Rev. Fluids* **2** (11), 114501.
- WU, J., LESTER, D., TREFRY, M.G. & METCALFE, G. 2024 Lagrangian coherent structures control solute dispersion in heterogeneous poroelastic media. *Phys. Rev. Fluids* **9**, 044501.
- WU, J., LESTER, D.R., TREFRY, M.G. & METCALFE, G. 2020 When do complex transport dynamics arise in natural groundwater systems? *Water Resour. Res.* **56** (2), e2019WR025982.
- YE, Y., CHIOGNA, G., CIRPKA, O.A., GRATHWOHL, P. & ROLLE, M. 2015 Experimental evidence of helical flow in porous media. *Phys. Rev. Lett.* **115**, 194502.
- YOMDIN, Y. 1987 Volume growth and entropy. *Israel J. Maths* **57** (3), 285–300.
- YOSHIDA, Z. 2009 Clebsch parameterization: basic properties and remarks on its applications. *J. Math. Phys.* **50** (11), 113101.

- YOSHIDA, Z. & MORRISON, P.J. 2017 Epi-two-dimensional fluid flow: a new topological paradigm for dimensionality. *Phys. Rev. Lett.* **119**, 244501.
- ZECH, A., ATTINGER, S., BELLIN, A., CVETKOVIC, V., DIETRICH, P., FIORI, A., TEUTSCH, G. & DAGAN, G. 2019 A critical analysis of transverse dispersivity field data. *Ground Water* **57** (4), 632–639.